

**ADVANCING HYPERSPECTRAL SOUNDER  
APPLICATIONS IN ANALYSIS OF  
PYROCUMULONIMBUS EVENTS**

*by*

Rebecca E. Schultz

A thesis submitted in partial fulfillment of the  
requirements for the degree of

Master of Science

Atmospheric and Oceanic Sciences

*at the*

UNIVERSITY OF WISCONSIN – MADISON

2017

APPROVED

---

Professor, Atmospheric and Oceanic Sciences

---

Date

## **Abstract**

Hyperspectral sounder measurements from instruments such as the Atmospheric Infrared Sounder (AIRS) aboard the EOS-Aqua satellite, the Cross-track Infrared Sounder (CrIS) aboard the Suomi-NPP satellite, and the Infrared Atmospheric Sounding Interferometer (IASI) aboard the MetOp-A and MetOp-B satellites, are capable of retrieving temperature and humidity profiles at high vertical resolution. With the use of these polar-orbiting sensors, this study focuses on the most extreme of severe pyroconvection events, called Pyrocumulonimbus (PyroCb), in which the plumes can grow within hours to impact the upper troposphere and lower stratosphere. The impacts of such events are of relevance to stratospheric chemistry, aviation, and the global climate. The atmospheric environment preceding these short-lived PyroCb events can be observed and diagnosed through the use of hyperspectral retrievals with greater spatial and temporal precision than available from the routine observation network. This study aims to analyze the state of the atmosphere throughout the lifecycle of a PyroCb event in order to better understand the evolution and structure of PyroCb clouds.

Hyperspectral sounder temperature and moisture retrievals are used in this study to investigate PyroCb development during the Yarnell Hill Wildfire in Yarnell, Arizona during June 2013 and the Fort McMurray Wildfire in Fort McMurray, Alberta during May 2016. We aim to demonstrate the potential use of these hyperspectral sounder measurements and retrievals in the characterization and analysis of PyroCb events, as well as for real-time environmental monitoring and forecasting purposes.

## **Acknowledgments**

No individual reaches the completion of a Master's degree without a team of support behind them. I am no exception. I would first like to thank my academic advisor, Dr. Michael C. Morgan, for his incredible guidance and valuable advice throughout my academic career. His work ethic is unparalleled, and he has helped shape me into the hardworking, passionate student that I am today. I would also like to thank my research advisor, Dr. Elisabeth Weisz, for providing me the opportunity to pursue this project for my graduate studies. She has been a true mentor throughout this process and I am so grateful for her direction. It has been an honor call myself a student of both of these brilliant individuals. I am also grateful to Dr. Bryan Baum for his support and involvement in this project, and for insightful conversations and correspondence with Dr. Michael Fromm and Dr. David Peterson (Naval Research Laboratory). I would be remiss if I did not thank my reviewers, as well: Dr. Brett Hoover and Dr. Jonathan E. Martin. I am thankful to have had the friendship and support of the Martin and Morgan research groups, whose fascinating research presentations made early morning meetings enjoyable. I am grateful to have been a part of both the AOS Undergraduate Class of 2015 and the AOS Graduate Class of 2017, each full of exceptionally supportive and intelligent people that I am lucky to now call my friends. Lastly, I must thank my family for allowing me to chase this dream. Their support has guided me through my eleven semesters at the University of Wisconsin-Madison.

The research reported in this thesis was supported by the NOAA Joint Polar Satellite Systems (JPSS) Proving Ground Risk Reduction (PGRR) program under NOAA Contract No. NA15NES4320001.

## Table of Contents

Abstract.....	i
Acknowledgments.....	ii
Table of Contents.....	iii
List of Figures.....	v
List of Tables.....	ix
List of Equations.....	x
1 Introduction.....	1
1.1 Satellite Remote Sensing.....	1
1.2 Pyrocumulonimbus Events.....	2
2 Background and Motivation.....	4
2.1 Radiative Transfer.....	4
2.1.1 Planck Function and Wien’s Displacement Law.....	6
2.1.2 The Radiative Transfer Equation (RTE).....	7
2.1.3 Brightness Temperature.....	9
2.2 Hyperspectral Sounders.....	12
2.2.1 Atmospheric Infrared Sounder (AIRS).....	13
2.2.2 Infrared Atmospheric Sounding Interferometer (IASI).....	14
2.2.3 Cross-track Infrared Sounder (CrIS).....	15
2.3 Pyrocumulonimbus (PyroCb) Events.....	17
2.3.1 Peterson Classifications.....	19
3 Data and Models.....	22

3.1	Linear Regression .....	23
3.2	Physical Optimal Estimation.....	25
3.3	Specific Retrieval Algorithms.....	27
3.3.1	Dual Regression (DR).....	27
3.3.2	NOAA Unique Combined Atmospheric Processing System (NUCAPS) .....	29
3.3.3	AIRS L2 Standard Physical Retrieval.....	34
3.4	Weather Research and Forecasting (WRF) Model .....	35
3.5	Additional Data Sources .....	41
4	Case Studies .....	42
4.1	Yarnell Hill Wildfire.....	42
4.2	Fort McMurray Wildfire.....	55
5	Summary and Conclusions .....	74
	References.....	78

## List of Figures

1	Observed radiances from Metop-A IASI, 03 May 2016, across a portion of the electromagnetic spectrum. ....	5
2	Observed brightness temperatures from Metop-A IASI, 03 May 2016, across a portion of the electromagnetic spectrum. ....	10
3	Brightness temperature observations at 10.9 $\mu\text{m}$ from Metop-A IASI, 03 May 2016, across western Canada (above); brightness temperature spectra at selected locations across western Canada (below).....	11
4	Dual Regression retrieval algorithm schematic diagram. Adapted from Figure 1 of Weisz (2015b). “FM” refers to the “forward model” used for radiative transfer calculations. ....	30
5	NUCAPS retrieval algorithm schematic diagram. Adapted from NUCAPS ATBD.....	33
6	AIRS L2 Standard Physical Retrieval algorithm schematic diagram. Adapted from AIRS L2 ATBD. ....	36
7	Domain configuration in WRF model for Fort McMurray case study. Outer domain denoted by black border. Inner (nested) domain denoted by white border. White dot inside nested domain denotes location of Fort McMurray wildfire.....	40
8	GOES-15 0.63- $\mu\text{m}$ visible image, 30 June 2013, 2345 UTC. Yarnell Hill PyroCb indicated by overshooting cloud top signature, outlined in red. ....	43
9	GEFS Reanalysis data for Yarnell Hill wildfire, 30 June 2013, at 1800 UTC. Black contours indicate 500-hPa geopotential heights in meters, contoured in 30-m intervals.	

	Shading indicates 500-hPa specific humidity in grams per kilogram, in 0.25-g kg <sup>-1</sup> intervals.....	44
10	Observed brightness temperature spectra for Yarnell Hill wildfire location, 30 June 2013, for (a) IASI-A at 1650 UTC; (b) CrIS at 1934 UTC; and (c) AIRS at 2111 UTC. ....	46
11	Brightness temperature observations at 10.9 μm 30 June 2013, across the southwestern United States, by (a) IASI-A at 1650 UTC; (b) CrIS at 1934 UTC; and (c) AIRS at 2111 UTC. Data in (b) interpolated to uniform 15-km grid. Location of Yarnell Hill wildfire denoted by a black plus sign. ....	48
12	Vertical profiles of (a) temperature, (b) relative humidity, and (c) specific humidity for each instrument during afternoon overpasses on 30 June 2013. Profiles retrieved using the Dual Regression retrieval algorithm. ....	49
13	Skew-T diagram with solid lines indicating temperature (in Celsius) and dashed lines indicating dew-point temperature (in Celsius). Black profiles denote AIRS retrieval from 2111 UTC 30 June 2013. Red profiles denote Flagstaff, Arizona radiosonde from 0000 UTC 01 July 2013. Blue profiles denote GDAS reanalysis at Yarnell from 0000 UTC 01 July 2013.....	52
14	Retrieved values of Convective Available Potential Energy (CAPE) (a,c) and Lifted Index (LI) (b,d) for CrIS and AIRS overpasses at 1934 UTC and 2111 UTC, respectively. Data interpolated to a uniform 15-km grid. Exact location of the Yarnell wildfire is denoted by a black plus sign.....	53

15	Visible images of Fort McMurray PyroCb event from (a) Aqua MODIS True Color at 1950 UTC 03 May 2016, left; and (b) Suomi-NPP VIIRS True Color at 2022 UTC on 03 May 2016. Red circles indicate location of PyroCb development.....	56
16	GEFS Reanalysis data for Fort McMurray wildfire, 04 May 2016, at 0000 UTC. Black contours indicate 500-hPa geopotential heights in meters, contoured in 30-m intervals. Shading indicates 500-mb specific humidity in grams per kilogram, in 0.25-g/kg intervals.....	57
17	Observed brightness temperature spectra at Fort McMurray, 03 May 2016, by (a) AIRS at 1947 UTC and (b) CrIS at 2018 UTC.....	59
18	Brightness temperature observations at 10.9 $\mu\text{m}$ , 03 May 2016, by (a) AIRS at 1947 UTC and (b) CrIS at 2018 UTC. Data interpolated to uniform 15-km grid. Location of Fort McMurray denoted by red circle. Black box and arrows in left figures denote region of zoom in right figures. ....	60
19	Vertical profiles of temperature (left), relative humidity (center), and specific humidity (right) retrieved from CrIS at 2018 UTC 03 May 2016, using (a) the Dual Regression algorithm and (b) the NUCAPS algorithm. Red profiles in (a) represent the mean of the nine profiles in blue, calculated in order to match the resolution in (b). ....	62
20	Retrieved profiles of (a) temperature, (b) relative humidity, and (c) specific humidity. Red profiles represent AIRS L2 retrieval at 1947 UTC, 03 May 2016. Blue profiles represent CrIS NUCAPS retrieval at 2018 UTC, 03 May 2016. Green profiles represent CrIS DR retrieval at 2018 UTC, 03 May 2016.....	63
21	Radiosonde locations nearest location of the Fort McMurray wildfire. ....	66

- 22 Skew-T diagram comparing the AIRS L2 retrieval of the AIRS 1947 UTC overpass to (a) an 1800 UTC radiosonde from Edmonton, and (b) 0000 UTC radiosondes from Edmonton, Fort Nelson, and Fort Smith. Solid profiles denote temperature. Dashed profiles denote dew-point temperature. .... 67
- 23 WRF model output, 03 May 2016, valid (a) 1800 UTC, (b) 1900 UTC, (c) 2000 UTC, and (d) 2100 UTC. Black contours denote 700-hPa geopotential height, contoured in 3-hPa intervals. Shading denotes mixing ratio, contoured in  $0.4\text{-g kg}^{-1}$  intervals from  $2.4\text{-g kg}^{-1}$  to  $5.2\text{-g kg}^{-1}$ . Wind barbs (blue) denote observed wind in kts. Black plus sign denotes location of Fort McMurray wildfire. .... 69
- 24 Skew-T diagram of AIRS L2 retrieval valid 1947 UTC (red) and WRF output valid 2000 UTC (blue) at location of Fort McMurray wildfire 03 May 2016. Solid lines indicate temperature in degrees Celsius. Dashed lines indicate dew-point temperature in degrees Celsius..... 71
- 25 Time-height plot of hourly WRF output from 1600 UTC - 2200 UTC, 03 May 2016. Pink contours denote mixing ratio, in  $\text{g kg}^{-1}$ , contoured in  $0.5\text{-g kg}^{-1}$  intervals. Orange wind barbs denote observed winds in kts. .... 72

## List of Tables

- 1 Table 1: Specifications of hyperspectral sounders AIRS, IASI, and CrIS. .... 16
- 2 Table 2: Specifications of retrieval algorithms DR, NUCAPS, and AIRS L2. .... 37

## List of Equations

1	(2.1) Planck function.....	6
2	(2.2) Wien's Displacement Law. ....	6
3	(2.3) Upwelling radiation observed from space.....	7
4	(2.4) Emission weighting function.....	8
5	(2.5) Brightness Temperature. ....	9
6	(3.1) Linear regression model.....	24
7	(3.2) Linear regression coefficients .....	24
8	(3.3) Maximized physical optimal estimation solution.....	26
9	(3.4) Error covariance. ....	26

# **1 Introduction**

## **1.1 Satellite Remote Sensing**

Satellite data has had an increasingly profound effect on the earth science community for the last five decades. Weather prediction and forecasting is a particular facet of the earth sciences that has benefited immensely from such data, with analysis and forecast improvement advancing in conjunction with the technological advancement of new satellites and as techniques are developed to derive and assimilate an ever-wider spectrum of meteorological observations from satellite platforms. Satellites sense outgoing electromagnetic radiation from the earth's atmosphere; this radiation leaving the earth's atmosphere varies with wavelength, and satellites fundamentally measure this radiation across the electromagnetic spectrum, most specifically within the microwave and infrared bands. These radiation measurements prove incredibly useful as various atmospheric parameters can be inferred from them, including atmospheric gas concentrations, brightness temperatures, surface emissivity, and cloud optical depth.

The earliest satellites launched in the 1960's were polar-orbiting satellites, orbiting in a sun-synchronous pattern and therefore passing almost all locations on the planet twice per day. These satellites produced visible imagery and infrared radiometry, giving scientists the first global picture of the earth's surface in 1964. The implementation of geostationary orbiting satellites a short decade later advanced satellite meteorological capabilities further with their ability to produce observations at much smaller time increments. Shortly thereafter, technologies improved and emphasis shifted to include measurements of the vertical temperature and moisture structure of the atmosphere. King (1958) and Kaplan

(1959) conducted research that suggested the possibility of inferring from infrared radiometry atmospheric temperature as a function of the associated atmospheric pressure level, leading to the first satellite-derived temperature profile retrievals in 1969. These atmospheric vertical profiles, specifically of temperature and moisture, have since become valuable analytical and diagnostic tools useful to weather prediction and forecasting.

Modern meteorological satellites carry a suite of onboard instruments, including imagers, sounders, radiometers, and various gas and aerosol monitors, among others. Hyperspectral sounders are remote sensing instruments that measure the earth's upwelling radiation in thousands of narrow bandwidth channels. The high spectral resolution of these measurements allows for the retrieval of high vertical resolution atmospheric profiles. Hyperspectral sounder radiance can be inverted into vertical profiles of temperature, moisture, and ozone, as well as various surface and cloud parameters. Their placement aboard polar-orbiting satellites provides extensive global coverage with twice-daily overpasses, thus providing measurements over regions where traditional in-situ observation networks (e.g., radiosondes, aircraft observations, surface observations) are sparse. Four hyperspectral sounders are currently in orbit, each collecting observations over the same location within hours of one another, and using data from each of these instruments allows for studies of time tendency of various atmospheric phenomena.

## **1.2 Pyrocumulonimbus Events**

Pyrocumulonimbus (PyroCb) activity is a primary focus of this study. PyroCb are intense, fire-initiated thunderstorms that are capable of injecting large amounts of smoke and ash into the upper-troposphere/lower-stratosphere (UTLS) (Fromm, 2010). They are extreme

forms of deep pyroconvection, and widely observed in remote regions of the western United States and Canada, as well as in parts of Russia and western Australia. Much work has been done by Dr. Michael Fromm and Dr. David Peterson of the Naval Research Laboratory (NRL) to detect, analyze, and characterize these PyroCb events over the last decade.

Nevertheless, these PyroCb events are widely understudied. As a consequence, investigating and describing the antecedent environmental conditions for these events using hyperspectral sounder data serves as the focus for this study. The goals of this study are to: 1) demonstrate the extent and capability of the hyperspectral sounder dataset; 2) describe the atmospheric environment before, during, and after PyroCb development; and 3) compare and contrast hyperspectral retrieved profiles with other existing data sources and model output. Section 2 provides an introduction to radiative transfer and details how radiance measurements are used to calculate brightness temperatures. Also described in this section are the three hyperspectral sounders that are currently in orbit, as well as a brief literature review of PyroCb activity. Section 3 gives a broad overview of both linear regression and physical optimal estimation before describing in detail the three retrieval algorithms used in this study. The WRF model is also introduced and summarized in this section. Section 4 presents in detail two separate case studies conducted in this research: the first is a wildfire in Yarnell, Arizona during June 2013, and the second is a wildfire in Fort McMurray, Alberta during May 2016. Section 5 serves as a summary of the research presented and draws conclusions thereafter.

## 2 Background and Motivation

### 2.1 Radiative Transfer

A solid understanding of how radiation is measured as it leaves the earth-atmosphere system is an essential foundation to the study of hyperspectral retrievals. Radiation is defined as the process by which energy is transferred across space without the necessity of a transfer medium (Menzel, 2006). Meteorological remote sensing is the passive detection of this radiation leaving the earth system by satellites (Petty, 2006). Radiation upwelled from the earth system varies with wavelength across the electromagnetic spectrum. It is estimated that 99% of the radiation leaving the atmosphere is found in the thermal infrared band from 4-100  $\mu\text{m}$  (Petty, 2006). Figure 1 is an example of the observed terrestrial radiance spectrum, with the maximum radiance values occurring between 10 – 12.5  $\mu\text{m}$  (800 to 1000  $\text{cm}^{-1}$ ). Vertical profiles are derived near bands where atmospheric gases are absorbed. Measurements taken at the center of an absorption band represent radiation from the upper atmosphere (as radiation from lower levels has been absorbed by these gases), and measurements taken away from the center of an absorption band represents radiation from lower levels of the atmosphere (Menzel, 2006). These parts of the electromagnetic spectrum with high transparency, where no absorption occurs, are referred to as “window regions,” as measurements from these regions represent a full vertical sampling of the atmosphere.

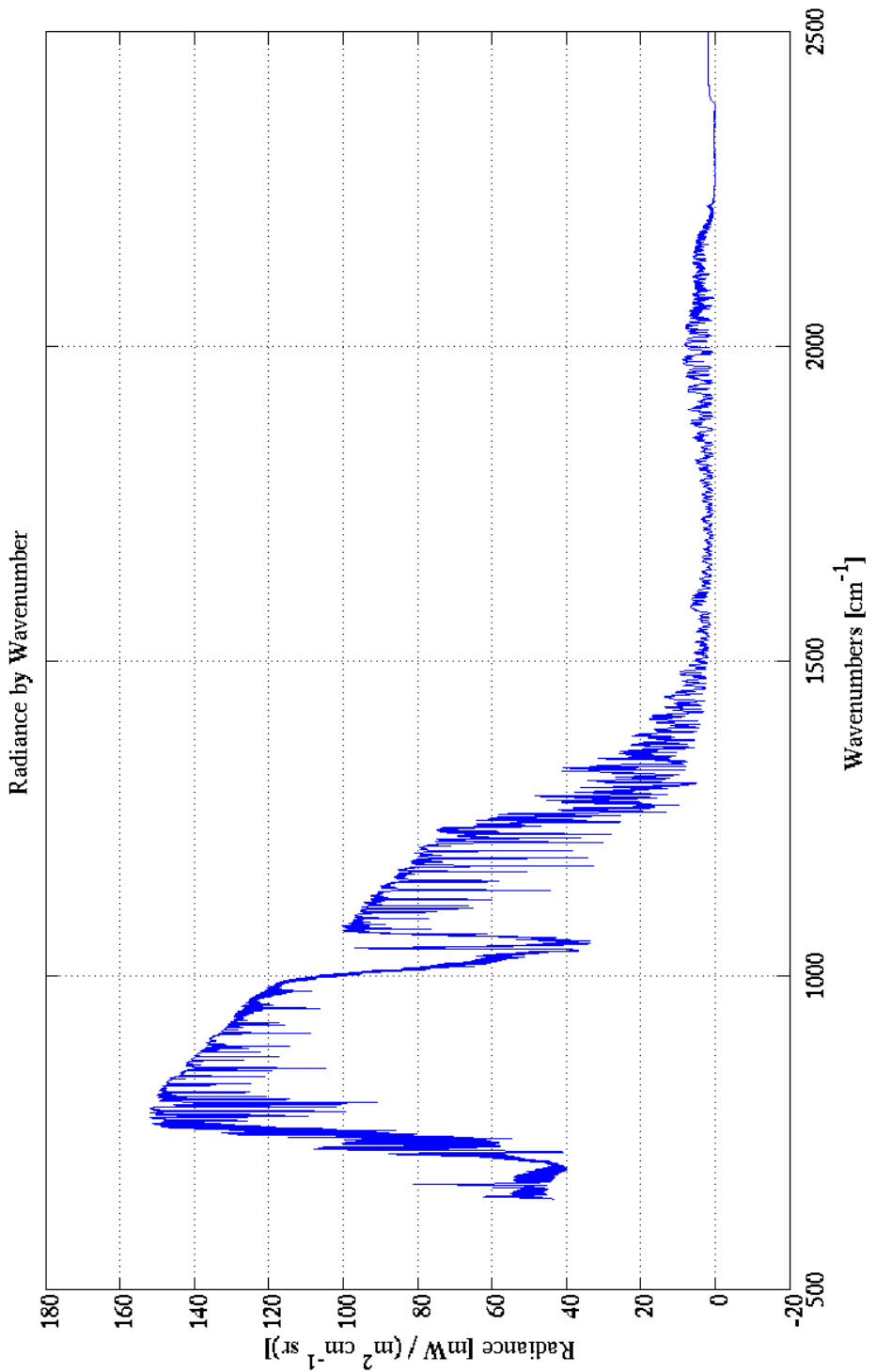


**Figure 1:** Observed radiances from Metop-A IASI, 03 May 2016, across a portion of the electromagnetic spectrum.

### 2.1.1 Planck Function and Wien's Displacement Law

In addition to absorption by various gases within the atmosphere, variations in radiation by wavelength are described by the Planck function dependence on wavelength (Menzel, 2006). An object with a given absolute temperature emits radiation at all possible wavelengths, and it is important to understand that there is a “hard upper bound on the amount of radiation” at any given wavelength (Petty, 2006). Thus, the Planck function describes this upper limit as a function of temperature and wavelength. It is given as follows:

$$B_{\lambda}(T) = \frac{2hc^2}{\lambda^5 \left( \exp\left(\frac{hc}{k_B \lambda T}\right) - 1 \right)} \quad (2.1)$$

where  $h = 6.626 \times 10^{-34}$  J s is Planck's constant,  $c = 2.998 \times 10^8$  m s<sup>-1</sup> is the speed of light, and  $k_B = 1.381 \times 10^{-23}$  J K<sup>-1</sup> is Boltzmann's constant. The units for  $B_{\lambda}(T)$  are that of intensity per unit solid angle, most commonly seen as W m<sup>-2</sup> μm<sup>-1</sup> sr<sup>-1</sup>.

The Planck function is formally defined as the intensity of radiation emitted by a blackbody at a given wavelength (Petty, 2006). A blackbody is an object that absorbs radiation perfectly, and serves as a reasonable approximation for thermal emission. There is an inverse relationship between an object's temperature and the wavelength at which the Planck function peaks, i.e. a cool object's peak thermal emission will occur at a much longer wavelength than a warm object. This relationship is described by Wien's Displacement Law:

$$\lambda_{\max} = \frac{k_w}{T} \quad (2.2)$$

where  $k_w = 2897$  μm K. This law is most informative for identifying where peak emission falls in the electromagnetic spectrum for objects of a given temperature. For instance,

standard atmospheric temperatures ranging from 200 K – 300 K bear peak emission between 9.6  $\mu\text{m}$  and 14.4  $\mu\text{m}$ , in the thermal infrared band. Additionally, standard solar temperatures near 6000K bear peak emission near 0.5  $\mu\text{m}$ , in the visible band (Petty, 2006).

### 2.1.2 The Radiative Transfer Equation (RTE)

In the field of remote sensing, the Planck function is used most commonly in describing upwelling radiation from the earth system. This radiation can be described as the sum of two parts: the first being the contribution of radiation emitted from the surface of the earth, and the second being the contribution of radiation from each level of the atmosphere. The surface of the earth is assumed to be a blackbody. Upwelling radiation leaving the atmosphere that can be sensed by satellite-borne instruments is described by the following equation:

$$I^\uparrow(\infty) = B_\lambda(T_s)t^* + \int_0^\infty (B_\lambda[T(z)])(W^\uparrow(z))dz \quad (2.3)$$

The first term on the right-hand side of this equation,  $B_\lambda(T_s)t^*$ , represents the surface contribution of radiation, using the Planck function with surface temperature,  $T_s$ , and the total transmittance,  $t^*$ , which is defined as the ratio of effectiveness of transmitting radiant energy from the surface to the top of the atmosphere (Petty, 2006). The second term on the right-hand side (2.3) represents the radiation from each level of the atmosphere between the surface and the space-borne instrument, thus incorporating the indefinite integral from the surface to infinity. The first term inside this integral,  $B_\lambda[T(z)]$ , uses the Planck function to measure intensity of radiation at every level  $z$ , represented by  $T(z)$ . The second term is called the emission weighting function, which is defined as the following:

$$W^\uparrow(z) = \frac{dt(z, \infty)}{dz} = \frac{\beta_a(z)}{\mu} t(z, \infty) \quad (2.4)$$

where  $\beta_a$  represents the absorption coefficient and  $\mu = |\cos \theta|$  represents the path length determined by the solar angle. This function, the derivative of transmittance with respect to height, physically characterizes the relative contribution of each atmospheric layer on the total amount of radiation emitted to space. Thus, a weighting function can be calculated at each wavelength on a given spectrum, providing insight into which atmospheric layer the radiation at that wavelength originated. In remote sensing, a satellite sensor capable of measuring radiant intensities,  $I_i$ , over closely spaced wavelengths,  $\lambda_i$ , on the edge of an absorption band will have each channel measure radiation from a specific atmospheric layer (Petty, 2006). Recall that measurements taken directly at the center of an absorption band represent radiation from the upper atmosphere, and measurements taken away from the center represent radiation from lower levels. Thus, gathering measurements from both regions of an absorption band will yield a full vertical profile of the atmosphere at various levels. The weighting functions of each instrument channel are of great importance to this study, as the information these functions contain will guide the process of retrieval for vertical temperature and moisture profiles. An in depth description of this process is presented in Chapter 3. It is important to note that equations 2.3 and 2.4 represent upwelling radiation measured by a space-borne instrument. A separate set of equations governs the measurement of downward radiation by a surface-based instrument.

### 2.1.3 Brightness Temperature

The relationship between intensity and blackbody temperature as described by the Planck function allows for the conversion of intensity into brightness temperature,  $T_B$ :

$$T_B \equiv B_\lambda^{-1}(I_\lambda) \quad (2.5)$$

where  $B_\lambda^{-1}$  is the inverse of the Planck function applied to the observed radiance. Brightness temperature is formally defined as the equivalent blackbody temperature of a given intensity, and is used as a reliable substitute for physical temperature in radiative transfer calculations (Petty, 2006). Because dense cloud layers and land and water surfaces have high emissivity in the thermal infrared band, brightness temperatures calculated for these surfaces compare very closely to actual, physical temperatures of these surfaces. However, where emissivity is low, such as over glacial ice observed in the microwave band, brightness temperatures do not compare well with the actual temperature. Figure 2 shows observed brightness temperatures across a range of wavenumbers observed by the IASI instrument, with maximum values occurring in the transparent window region between wavenumbers of 800 and 1000  $\text{cm}^{-1}$ . Similarly, Fig. 3 shows brightness temperatures observed by IASI at one selected wavenumber across varying landscapes and cloud features noted on the map of western Canada. The full spectra at selected locations are shown as well. Brightness temperatures are much colder across the entire spectrum for the case of a high, cold cloud like 'B', whereas they are much warmer for the case of a cloud-free surface observation like 'A'.

The importance of radiative transfer to remote sensing and satellite applications cannot be overstated, as the presented material lays a foundation for the use of hyperspectral sounder retrievals in the analysis of Pyrocumulonimbus events. However, the subject of

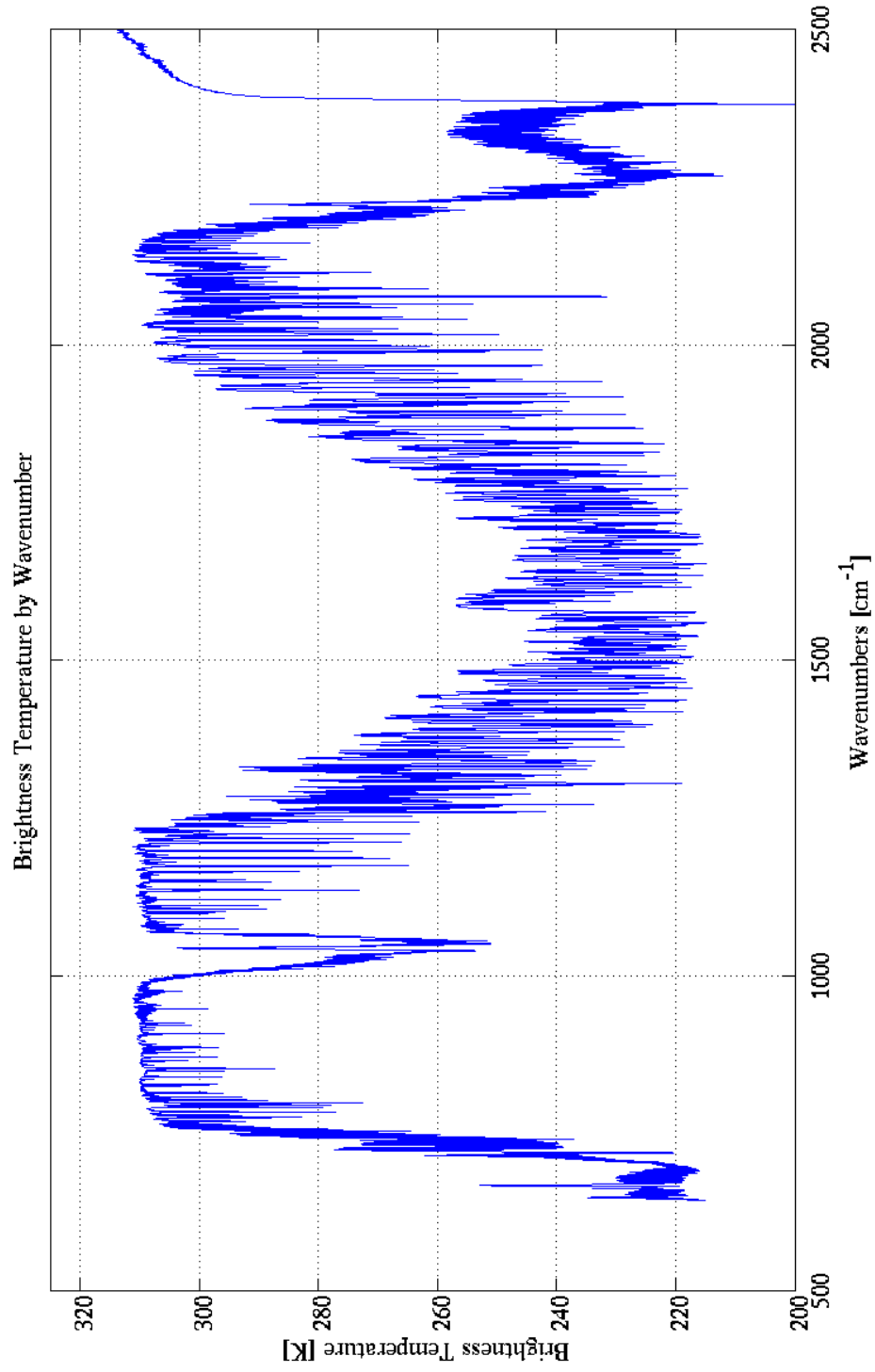


**Figure 2:** Observed brightness temperatures from Metop-A IASI, 03 May 2016, across a portion of the electromagnetic spectrum.

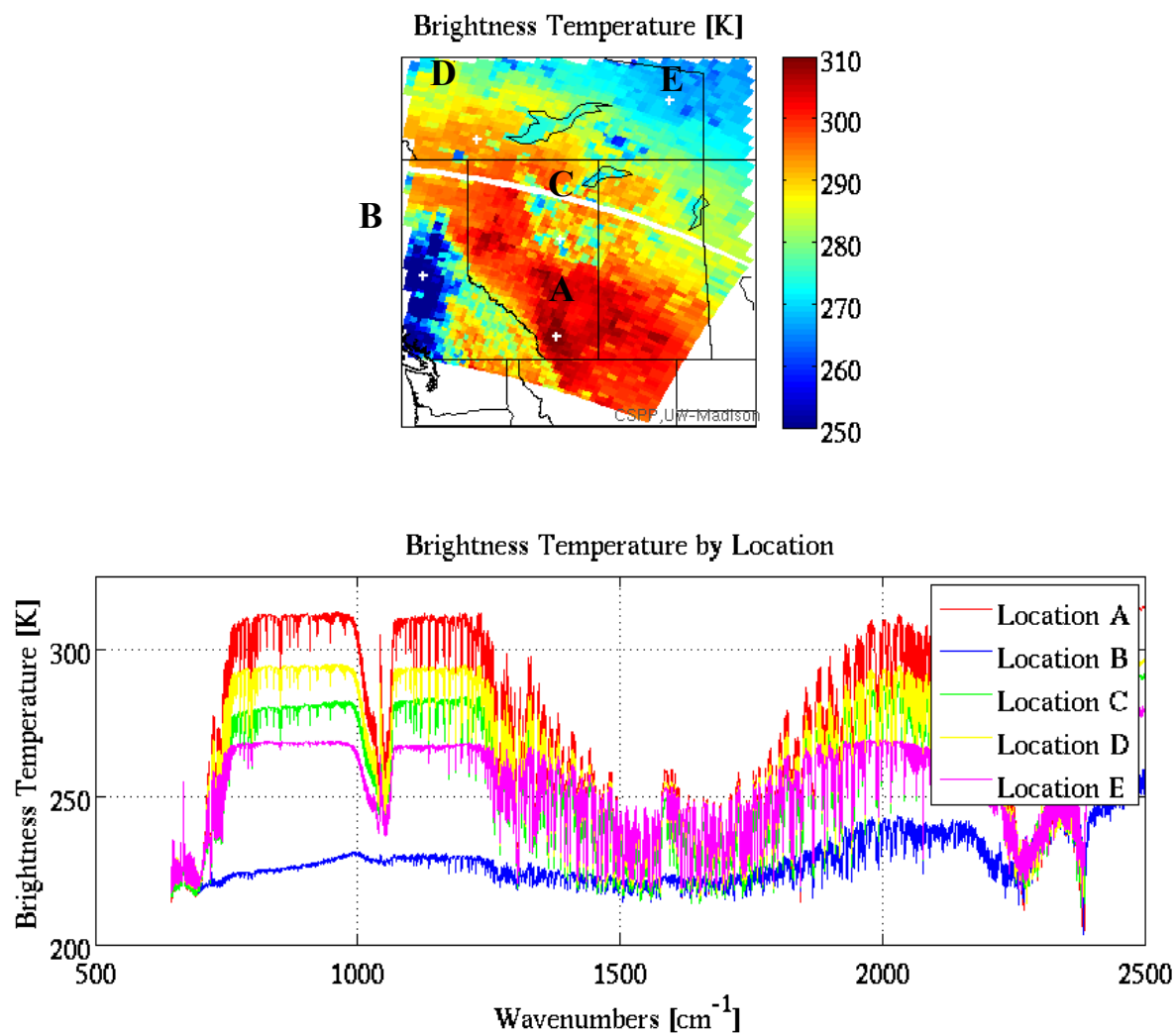


**Figure 3:** Brightness temperature observations at 10.9  $\mu\text{m}$  from Metop-A IASI, 03 May 2016, across western Canada (above); brightness temperature spectra at selected locations across western Canada (below).

radiative transfer as a whole, with its associated equations, derivations, and explanations, is far too expansive to successfully address here. This brief and general overview of how radiative transfer is used in this study shall suffice for the scope of this research.

## 2.2 Hyperspectral Sounders

A sounder is an instrument that acquires multispectral measurements from which vertical profiles of atmospheric temperature and humidity can be derived<sup>1</sup>. These instruments measure from space the radiation leaving the earth system. Measurements of radiation from these instruments are referred to as “Level 1” data products. These instruments operate most commonly in the microwave and infrared bands of the electromagnetic spectrum, and they are not exclusive to polar-orbiting satellites. Geostationary orbiting sounders play an important role in modern remote sensing (Menzel, 2006). Examples of traditional (i.e. non-hyperspectral) sounders include the Advanced Microwave Sounding Unit (AMSU-A) aboard the NOAA Aqua satellite, which features fifteen channels, and the Visible Infrared Imaging Radiometer Suite (VIIRS) aboard the Suomi-NPP satellite, featuring 21 channels.

In contrast, hyperspectral sounders are instruments that measure top-of-atmosphere (TOA) radiation in thousands of narrow bandwidth channels, most frequently in the infrared band<sup>1</sup>. This increase in spectral resolution by nearly two orders of magnitude makes hyperspectral sounder measurements an extremely valuable dataset. High spectral resolution translates to increased sensitivity to changes in the vertical atmospheric column, making the vertical profiles of hyperspectral sounders much more detailed than that of traditional

---

<sup>1</sup> American Meteorological Society, cited 2017. Glossary of Meteorology. <http://glossary.ametsoc.org>.

sounders. A total of three different hyperspectral sounders are currently in orbit aboard polar-orbiting satellites, providing the potential for vertical temperature and moisture profiles at any location on the planet twice per day. The three hyperspectral sounders currently in orbit are the instruments of focus for this research, and are described in detail in the following sections, and also summarized in Table 1.

### **2.2.1 Atmospheric Infrared Sounder (AIRS)**

The Atmospheric Infrared Sounder (AIRS) was first launched into orbit on 4 May 2002 aboard NASA's EOS Aqua satellite. AIRS is one of six different instruments aboard Aqua, and is often used in conjunction with the microwave sounder AMSU-A to obtain measurements from the same time and location in the microwave and infrared. This cross-track scanning instrument is a grating spectrometer, which features a scan mirror that scans in a path perpendicular to the flight path of the satellite and directs upwelling radiation from the earth system into the instrument<sup>2</sup>. The mirror creates a swath of roughly 800 km on each side of nadir, and operates at an altitude approximately 700 km above earth. The instrument has a scan period of 2.667 seconds.

Additionally, AIRS features 2378 channels, which gives the instrument its hyperspectral sounder classification. It features a spectral resolution of  $0.5 - 2.0 \text{ cm}^{-1}$ , and a spectral range of  $650 - 2670 \text{ cm}^{-1}$  ( $15.4 \text{ }\mu\text{m} - 3.7 \text{ }\mu\text{m}$ ). At nadir, the instrument has a spatial resolution of approximately 13.5 km, sometimes referred to as the instantaneous field-of-view (IFOV) which is circular in shape. It is important to note that AIRS Physical Standard

---

<sup>2</sup> The AIRS Instrument Suite, 2013. NASA Jet Propulsion Laboratory.  
<http://airs.jpl.nasa.gov>.

Retrievals, or Level 2 products, use a 3x3 field-of-view (FOV) array that extends the spatial resolution to 40.5 km, three times that of the IFOV. This use of a 3x3 FOV array will be addressed more thoroughly in Chapter 3. More information on the AIRS instrument can be found at <http://airs.jpl.nasa.gov>.

### **2.2.2 Infrared Atmospheric Sounding Interferometer (IASI)**

The first launch of the Infrared Atmospheric Sounding Interferometer (IASI) was on 19 October 2006 aboard EUMETSAT's Metop-A satellite. A second IASI instrument with identical characteristics was launched into orbit on 17 September 2012 aboard EUMETSAT's Metop-B satellite. Thus, the two IASI instruments will be referred to hereafter as IASI-A and IASI-B, in relation to their respective satellites. A third IASI instrument is scheduled for launch in 2018.

IASI is a Michelson Interferometer, as opposed to a grating spectrometer used in AIRS, and has a cross-track scanning system that moves in a direction perpendicular to that of the flight path of the satellite. The instrument creates a swath of roughly 1100 km on each side of nadir and is situated roughly 820 km above the earth<sup>3</sup>. The scan period is approximately 8 seconds. IASI features an incredible 8461 channels, nearly four times that of AIRS. It has a spectral resolution of  $0.25 \text{ cm}^{-1}$  and a spectral range of  $645 - 2760 \text{ cm}^{-1}$  ( $15.5 \text{ }\mu\text{m} - 3.62 \text{ }\mu\text{m}$ ). At nadir, the instrument has a spatial resolution, or IFOV, of 12 km. More information on the IASI instruments can be found at <http://www.eumetsat.int>.

---

<sup>3</sup> IASI. EUMETSAT. <http://www.eumetsat.int/>

### 2.2.3 Cross-track Infrared Sounder (CrIS)

The Cross-track Infrared Sounder (CrIS) was launched into orbit on 28 October 2011 aboard NOAA's Suomi-NPP satellite. CrIS is one of five instruments aboard Suomi-NPP, and complements the microwave radiometer ATMS. The instrument is a Michelson Interferometer, similar to IASI, with a cross-track scanning system that moves in a direction perpendicular to the flight path of the satellite<sup>4</sup>. As it scans, CrIS creates a swath roughly 1100 km on each side of nadir, and has an altitude of approximately 825 km.

Additionally, CrIS features 1305 channels, just over half of the channels on AIRS and nearly one seventh of the channels on IASI. It has a spectral resolution of  $0.625\text{ cm}^{-1}$  for long-,  $1.25\text{ cm}^{-1}$  for mid-, and  $2.5\text{ cm}^{-1}$  for shortwave radiation, and a spectral range of  $650 - 2550\text{ cm}^{-1}$  ( $15.5\text{ }\mu\text{m} - 3.62\text{ }\mu\text{m}$ ). At nadir, the instrument features a spatial resolution, or IFOV, of roughly 14 km. It is worth noting that the algorithms presented in Chapter 3 will describe this IFOV differently than other instruments' IFOV, with one using a 3x3 FOV array to give a 42 km resolution, and the other keeping the 14 km IFOV for its spatial resolution. This process will be addressed more thoroughly in Chapter 3. More information on the CrIS instrument can be found at <http://www.jpss.noaa.gov/cris.html>.

Additionally, the technical specifications of each instrument are listed on Table 1.

---

<sup>4</sup> Cross-track Infrared Sounder (CrIS). NOAA Joint Polar Satellite System.  
<http://www.jpss.noaa.gov>.

<b>Instrument</b>	<b>AIRS</b>	<b>IASI</b>	<b>CrIS</b>
Satellite (Agency)	EOS Aqua (NASA)	Metop-A, Metop-B (EUMETSAT)	Suomi-NPP (NOAA)
Instrument Type	Grating Spectrometer	Michelson Interferometer	Michelson Interferometer
Launched	May 2002	Oct. 2006, Sept. 2012	Oct. 2011
No. of Channels	2378	8461	1305
Spectral Resolution	$0.5 - 2.0 \text{ cm}^{-1}$	$0.25 \text{ cm}^{-1}$	$2.5 \text{ cm}^{-1}$
Spectral Range	$650 - 2670 \text{ cm}^{-1}$ ( $15.4 - 3.7 \text{ }\mu\text{m}$ )	$645 - 2760 \text{ cm}^{-1}$ ( $15.4 - 3.9 \text{ }\mu\text{m}$ )	$650 - 2550 \text{ cm}^{-1}$ ( $15.5 - 3.62 \text{ }\mu\text{m}$ )
Spatial Resolution (at nadir)	13.5 km	14 km	12 km

**Table 1:** Specifications of hyperspectral sounders AIRS, IASI, and CrIS.

### 2.3 Pyrocumulonimbus (PyroCb) Events

Pyrocumulonimbus (PyroCb) events were chosen as the focus of study for several reasons. First, they are largely understudied, with fewer than 10 publications as of 2010. Second, they occur most commonly in remote regions, where traditional in-situ observations are sparse. Third, PyroCb events have the ability to inject large quantities of smoke and aerosols into the upper troposphere/lower stratosphere (UTLS) with implications for climate. And lastly, while several case studies on severe weather outbreaks (e.g., Weisz, 2015a; Weisz et al., 2013; Weisz, 2015b) had previously been conducted at the Cooperative Institute for Meteorological Satellite Studies (CIMSS) at the University of Wisconsin-Madison, there are no extant studies of PyroCb activity using hyperspectral sounder data.

PyroCb events are extreme, fire-initiated thunderstorms that have enough vertical extent to involve ice formation, lightning, and a resultant plume in the UTLS (Fromm, 2012). These storms are extreme forms of pyroconvection, characterized by distinctive cloud microphysics when compared with traditional convection (Peterson, 2017a). Latent heat release within the atmospheric column enables the convection within a PyroCb to reach the upper troposphere, and the large aerosol content yields extremely small cloud droplets. These small droplets “delay the onset of precipitation and evaporative cooling, potentially allowing an updraft to persist for a longer period of time than traditional convection” (Peterson, 2015). Fromm (2010) found that the robust updraft within the PyroCb is likely the most efficient method of vertical transport for recently emitted smoke particles to enter the UTLS. Fromm (2010) also found that in addition to a favorable Haines index (a fire-weather index derived from moisture and stability of the lower atmosphere intended to measure the intensification potential of a wildfire<sup>1</sup>), PyroCb development needs an initiation trigger; in

some cases, the heat and moisture from the fire itself is sufficient, but “occasionally the midlevel stability is too great for parcels to reach their level of free convection.” Thus, he notes that the passage of a cold front may help to enhance convection in these cases. Additionally, a study of the 2013 Rim Fire by Peterson (2015) showed a lack of PyroCb development within a dry atmospheric column, but strong PyroCb development in “an environment favorable for midlevel moisture entrainment and upper-level instability,” concluding that ambient midlevel moisture likely has an important role in PyroCb development.

The connection between stratospheric smoke layers and PyroCb activity was first identified in the early 2000s (Fromm, 2010); thus, these events have only begun being studied recently, unlike other atmospheric phenomena. These storms have a typical lifetime of approximately one hour, and reach their peak development and intensity in the late afternoon, likely due to trends in diurnal heating. PyroCb are also typically observed in remote regions, most prominently over the mid- to high-latitude forests of North America, Australia, and Asia. Due to their occurrence in these isolated areas, traditional in-situ observations are typically not available, and as a consequence, spaceborne observations are crucial to their study, detection, and investigation.

Much of the existing work on PyroCb activity has been conducted by a research group at the Naval Research Laboratory in Monterey, California, most prominently by Dr. Michael Fromm and Dr. David Peterson. The NRL team has focused the majority of their work thus far on wildfires in North America throughout the late 2000s and early 2010s.

Through his research on these cases, Dr. Fromm has seen two recurring themes emerge: first, that some “puzzling stratospheric aerosol-layer observations and other layers

reported as volcanic aerosol can now be explained in terms of pyroconvection”; and second, that PyroCb events occur surprisingly frequently and are likely a relevant aspect of several historic wildfires (Fromm, 2010). Peterson (2015) noted that the meteorological conditions driving large PyroCb events are still uncertain, and an automated, regional PyroCb detection system has still not been developed. Additionally, Peterson (2017a) again notes that PyroCb events “have not been studied over large spatiotemporal scales,” stating that the goal of his most recent studies has been “to improve systematic detection and characterization of these events through the development of an automated algorithm in western North America.” Thus, the additional study of these events is needed. Currently, a team of researchers at CIMSS maintains a blog-style database<sup>5</sup> of PyroCb activity as they are detected.

### **2.3.1 Peterson Classifications**

In an attempt to characterize the antecedent environments to PyroCb events, Peterson (2017b) created a conceptual model for development of intense PyroCb in western North America. Through his work, he analyzed 26 PyroCb events that occurred in North America during 2013, and identified three distinct classifications for the synoptic patterns during these PyroCb events: (1) the monsoonal anticyclone; (2) the West Coast disturbance; and (3) the Canadian ridge breakdown.

In the case of the monsoonal anticyclone, Peterson (2017b) notes that the southwestern portions of the continental United States (CONUS) “experiences a transition from a mid-latitude transient synoptic environment to the summer monsoonal pattern” during

---

<sup>5</sup> CIMSS PyroCb blog. Space Science and Engineering Center, University of Wisconsin-Madison. <http://pyrocb.ssec.wisc.edu>.

the months of May and June. An associated increase in surface heating forces a “northeastward migration, broadening, and flattening of the subtropical Pacific ridge,” or a “monsoonal anticyclone.” This synoptic pattern can combine with a low-level thermal trough, allowing for moisture advection from the tropical eastern Pacific and Gulf of Mexico. As the location and strength of this anticyclone varies over the summer season, the direction of moisture transport and associated position of convective development fluctuates, as well. Peterson (2017b) notes that of the 26 cases observed in 2013, nearly 62% (16 PyroCb events) were associated with the synoptic pattern of a monsoonal anticyclone.

The West Coast disturbance pattern is characterized by the leading edge of an approaching cyclone system off the West Coast of the United States. In this case, this “disturbance” near the coast, along with its associated frontal boundary, creates a pathway for the advection of subtropical midlevel moisture into central California over fires that are already burning downstream of this disturbance. Especially enhanced by elevated terrain, this pattern creates “an environment favorable for high-based convection”, the term “high-based” alluding to the higher altitude at which convective initiation takes place<sup>6</sup> (Peterson, 2017b). The aforementioned Peterson (2015) study of the 2013 Rim Fire was placed into this synoptic classification. Of the 26 cases observed in 2013, seven were associated with a West Coast disturbance pattern.

In the case of the Canadian ridge breakdown, Peterson (2017b) characterized a synoptic environment similar to the West Coast disturbance pattern, but focused in regions of western Canada with less complex topography and closer proximity to the polar jet.

---

<sup>6</sup> American Meteorological Society, cited 2017: "High-based thunderstorm". Glossary of Meteorology. <http://glossary.ametsoc.org>.

Typically, the boreal forests of western Canada experience “active fire seasons, periods of intense burning, and dry lightning strikes” often in the presence of a 500-hPa anticyclone (Peterson, 2017b). He notes, however, that fires tend to intensify most rapidly as the ridge associated with the anticyclone begins to breakdown. Such a process is commonly followed by the arrival of a surface cold front and an upper-tropospheric trough. Of the 26 cases observed across North America in 2013, all three Canadian events were associated with the Canadian ridge breakdown pattern.

In summary of his synoptic classifications, Peterson (2017b) states, “While regional variability is expected, all synoptic patterns [above] induce favorable fire weather conditions near the surface, [such as extremely warm temperatures and very dry conditions], along with mid- and upper-level [disturbances] favorable for convective [development].” These synoptic patterns are addressed again in Chapter 4, as they play a supportive role in investigating the atmospheric conditions with hyperspectral sounder data surrounding the two PyroCb case studies in this research.

### **3 Data and Models**

The Level 1 radiances measurements from the aforementioned hyperspectral sounders are informative and useful, but a second insightful dataset emerges when these Level 1 radiances are processed through a retrieval algorithm. These algorithms contain processes by which radiance values are inverted into vertical profiles of temperature and moisture from Level 1 radiances. In addition to vertical profiles, other products that come directly from these retrieval algorithms (often referred to as Level 2 data) include surface parameters, like skin temperature and surface emissivity; cloud parameters, like cloud-top altitude and effective cloud optical depth; and atmospheric concentrations of carbon dioxide and ozone.

The retrieval of vertical profiles of temperature and moisture allow for the calculation of other useful parameters, as well. These include dew-point temperature, total precipitable water (TPW), and instability values such as convective available potential energy (CAPE) or lifted index (LI). The ability to calculate these variables only expands the potential application of the hyperspectral sounder dataset, but these values also rely heavily on techniques embedded within these retrieval algorithms.

Weisz (2015a) defines a retrieval method as a technique most commonly designed to “maximize the signal-to-noise ratio and retrieve the best possible estimate (e.g., statistically the most probable solution) of the true atmospheric state,” from a collection of radiance observations across a range of channels whose vertical weighting functions penetrate through the atmosphere. Generally, these methods are based on either a linear regression or a physical optimal estimation approach. This chapter aims to clarify and understand such

techniques by providing a brief overview of the fundamental mathematics and statistics used in each algorithm before introducing the three used in this study.

### **3.1 Linear Regression**

Linear regression analysis is defined as the study of linear, additive relationships between variables; more colloquially, it is the method used to fit straight lines onto diverse patterns of data (Nau, 2014). Linear regression relies on a number of assumptions: (1) linearity, e.g. the expected value of a particular variable is a linear function of the given set of independent variables; (2) variations are independent random variables, e.g. unexplained variations are not auto-correlated if the variables are in a time series; (3) homoscedasticity, e.g. all variables have the same variance; and (4) the variables are normally distributed. While assuming the effects of nonlinearity to be negligible can seem like an extreme assumption for a regression model, often times nonlinearity does play a small enough role in a system for such a model to succeed. Linear regression is used as an inversion technique of satellite radiance measurements, with a long and proven success rate (e.g., Smith et al., 1970; Huang and Antonelli, 2001; Zhou et al., 2007; Weisz et al., 2007).

In remote sensing applications, linear regression as a statistical method uses pre-calculated coefficients to invert a radiance measurement into its statistically most probable atmospheric state (Weisz, 2015b). These regression coefficients for a retrieval algorithm are “calculated offline by correlating a diverse set of simulated (or measured) radiances with their coincident atmospheric profiles.” These radiances are often times then projected into principal components (or eigenvector) space, in order to preserve computational efficiency and information. By doing so, this allows for data compression and noise filtering, because

only the leading set of eigenvectors is used to represent the radiance measurement; applying these eigenvectors to the radiance spectrum yields so-called compressed radiances. The following equation represents the linear principal component regression model (or the linear least squares problem):

$$\mathbf{X} = \mathbf{C}\mathbf{A}^T \quad (3.1)$$

where  $\mathbf{X}$  represents the atmospheric variables,  $\mathbf{C}$  represents the regression coefficients, and  $\mathbf{A}^T$  (a non-square matrix) represents the compressed measurements  $\mathbf{A} = \mathbf{Y}\mathbf{U}$ , where  $\mathbf{Y}$  and  $\mathbf{U}$  represent the observations (measurements) and the leading set of eigenvectors, respectively.

The regression coefficients are calculated as:

$$\mathbf{C} = \mathbf{X} \mathbf{A} (\mathbf{A}^T \mathbf{A})^{-1} \quad (3.2)$$

In the regression retrieval process, these regression coefficients are calculated for a large training set of atmospheric profiles  $\mathbf{X}$  and associated simulated (with a radiative transfer forward model) radiance measurements  $\mathbf{Y}$ . To obtain the retrieval estimates, the same coefficients are then applied to real radiance measurements according to Eq. 2.1.

Weisz (2015b) mentions, however, that one potential weakness of a straightforward linear regression as a retrieval method is that it does not adequately account for the non-linear relationship between the measured radiance and the atmospheric state, in particular that produced by variable clouds and moisture. Linear regression serves as the foundational mechanism of the Dual Regression (DR) and AIRS retrieval algorithms described in the following sections.

### 3.2 Physical Optimal Estimation

Optimal estimation is a statistical technique that processes measurements to determine a minimum error estimate of the state of a system (Gelb, 1974). This technique does so by “utilizing knowledge of system and measurement dynamics, assumed statistics of system noises and measurement errors, and initial condition information.” Optimal estimation is beneficial in that it minimizes the estimation error in a well-defined statistical sense and it utilizes all measurement data, plus prior knowledge about the system. This method is largely based on Bayes theorem, which uses probability theory to describe the likelihood of an event (Rodgers, 2000). Rodgers (2000) describes the Bayesian approach to an inverse problem as follows:

“Before we make a measurement we have prior knowledge expressed as a prior *probability density function (pdf)*; the measurement process is expressed as a forward model which maps the state space into measurement space; Bayes’ theorem provides a formalism to invert this mapping and calculate a posterior *pdf* by updating the prior *pdf* with a measurement *pdf*.”

Rodgers (2000) notes that the Bayesian view is general; it is not just an inversion method which produces a solution, rather “it encompasses all inverse methods by providing a way of characterizing the class of possible solutions, considering all possible states, and assigning a probability density to each.”

As a retrieval method, physical optimal estimation utilizes location-specific prior information, as well as radiative transfer and weighting function calculations for every single FOV. The governing equation for the maximum *a posteriori* solution is as follows:

$$\hat{\mathbf{x}} = \mathbf{x}_a + \mathbf{S}_a \mathbf{K}^T (\mathbf{K} \mathbf{S}_a \mathbf{K}^T + \mathbf{S}_e)^{-1} (\mathbf{y} - \mathbf{K} \mathbf{x}_a) \quad (3.3)$$

where  $x_a$  represents a first-guess (background) estimate,  $S_a$  represents the background error covariance matrix,  $S_e$  represents the measurement error covariance matrix,  $y$  represents the measurements, and  $K$  represents the Jacobian matrix of the forward model<sup>6</sup>. The ultimate goal of the physical optimal estimation technique is to maximize the *pdf* and minimize the error covariance, thereby minimizing the differences by weighting them with error covariance. The covariance  $\hat{S}$  is given by:

$$\hat{\mathbf{S}} = (\mathbf{K}^T \mathbf{S}_e^{-1} \mathbf{K} + \mathbf{S}_a^{-1})^{-1} \quad (3.4)$$

These techniques of physical optimal estimation are most commonly applied to account for the nonlinearity of the retrieval, but are often computationally expensive, especially in the case of global or real-time forecasting using hyperspectral sounders (Weisz, 2015a). Physical optimal estimation is used in the NOAA Unique Combined Atmospheric Processing System (NUCAPS) retrieval algorithm described in the following sections.

It is important to note the difficulty in designing and developing a good retrieval algorithm. Weisz (2015a) lists the following challenges in doing so: (1) the inversion problem is under-constrained, since a near-continuous vertical profile must be retrieved from a finite number of spectral measurements; (2) the weighting functions feature particular widths, and often times overlap with one another, indicating a vertical correlation in the measurements “that makes exact characterization with high vertical resolution challenging”; and (3) the measurements always contain noise, limiting the achievable vertical resolution “through the spectral/vertical deconvolution on the radiance measurements.” These factors

---

<sup>6</sup> The forward model produces an estimate of what the observation would be based on the background state.

largely complicate the inversion of a multitude of measurements into an exact atmospheric profile. Thus, Weisz (2015a) emphasizes the need for these factors to be addressed in the retrieval method.

### **3.3 Specific Retrieval Algorithms**

The three algorithms used in this research are the Dual Regression (DR) algorithm, the NOAA Unique Combined Atmospheric Processing System (NUCAPS) algorithm, and the AIRS Level 2 Physical Standard Retrieval (AIRS L2) algorithm. While various algorithms exist, DR and NUCAPS were specifically chosen due to their software being freely available to the user community; AIRS L2 was chosen for a third point of comparison. Specifications of each algorithm are listed in Table 2.

#### **3.3.1 Dual Regression (DR)**

The Dual Regression (DR) algorithm was originally developed at the University of Wisconsin-Madison Space Science and Engineering Center (SSEC) during the early 1990s as a method to derive atmospheric temperature and moisture profiles from “the first hyperspectral radiance data obtained from aircraft” (Weisz, 2015a). Dual Regression was first publicly released as part of the Cooperative Institute for Meteorological Satellite Studies (CIMSS) Community Satellite Processing Package (CSPP) in November 2012. DR retrieves atmospheric parameters in real-time, regardless of surface and/or cloud condition, at single FOV resolution. It was designed with multi-instrument capability, e.g., for use with AIRS, IASI, and CrIS (Weisz, 2013). While the mathematical basis for Dual Regression is linear regression, DR handles the nonlinearity issue of the inversion problem better than traditional

regression by incorporating additional steps like cloud height classification. Its regression-based foundation also implies that the DR method does not rely on a location-specific estimate of the atmosphere, as it instead relies only on the variance and the mean of the atmospheric state from pre-calculated regression coefficients (Weisz, 2013). Smith (2012) calls Dual Regression a “fast, physical-statistical algorithm,” with the phrase “dual” referring to the utilization of two types of eigenvector [empirical orthogonal function (EOF)] regression coefficients: one for clear-sky conditions and one for cloudy conditions. These coefficients are computed once for each instrument.

The “clear-trained” regression involved with DR relates the surface and atmospheric-profile parameters to their associated calculated (i.e., simulated) radiance spectra. These spectra are produced by radiative transfer calculations that assume clear-sky atmospheric conditions. In contrast, the “cloud-trained” regression relates the surface, cloud, and atmospheric-profile parameters to their associated radiance spectra, which are calculated using a cloud radiative transfer model, which requires cloud parameters such as cloud height and cloud optical thickness as input. Both sets of regression coefficients are then applied to the observed radiance spectra for every FOV to achieve a clear and cloudy regression retrieval profile solution. The cloud top is then determined from the clear and cloudy temperature profiles and a collocated model profile (e.g., National Centers for Environmental Prediction (NCEP) Global Data Assimilation System). This is based on the concept that under clear conditions (and above clouds) both profiles are essentially the same, whereas under cloudy conditions the clear-trained retrieval will be colder than the cloud-trained solution below the cloud top (Smith, 2012; Weisz, 2013).

The Dual Regression algorithm then combines the clear-trained retrieval with the cloud-trained retrieval to produce accurate retrievals for both clear-sky and cloudy-sky conditions. Thus, the final profile retrieval “is taken as the clear-trained solution above the thermal-cloud-top level, and as the cloud-trained solution below the thermal-cloud-top-level” (Smith, 2012). It is important to note that since clouds hinder retrieval of geophysical information from space-based infrared (IR) instruments, profiles from below optically thick clouds are rejected (Weisz, 2015a). A schematic diagram adapted from Weisz (2015b) for the Dual Regression process is shown in Fig. 4.

Dual Regression has the processing capability of 25 – 75 FOVs per second, depending on available computational resources, and the entire suite of atmospheric parameters are provided for each FOV (Weisz, 2015a). The method features geophysical classification based on window region brightness temperatures, scanning angle, and cloud heights to account for nonlinearity between infrared radiances and the atmospheric state. The DR method uses the full information of hyperspectral sounder measurements, and because it does not depend on any background measurements (with the exception of the aforementioned GDAS profiles for determining cloud top), the retrievals are independent of any other data source and consistent in quality at every location (Weisz, 2015a).

### **3.3.2 NOAA Unique Combined Atmospheric Processing System (NUCAPS)**

The NOAA Unique Combined Atmospheric Processing System (NUCAPS) algorithm was originally developed as a method to retrieve vertical profiles of temperature and moisture from the AIRS/AMSU instrument suite measurements. However, NUCAPS was made freely available through CIMSS CSPP for retrievals of the CrIS/ATMS instrument

Pre-calculated for each instrument:

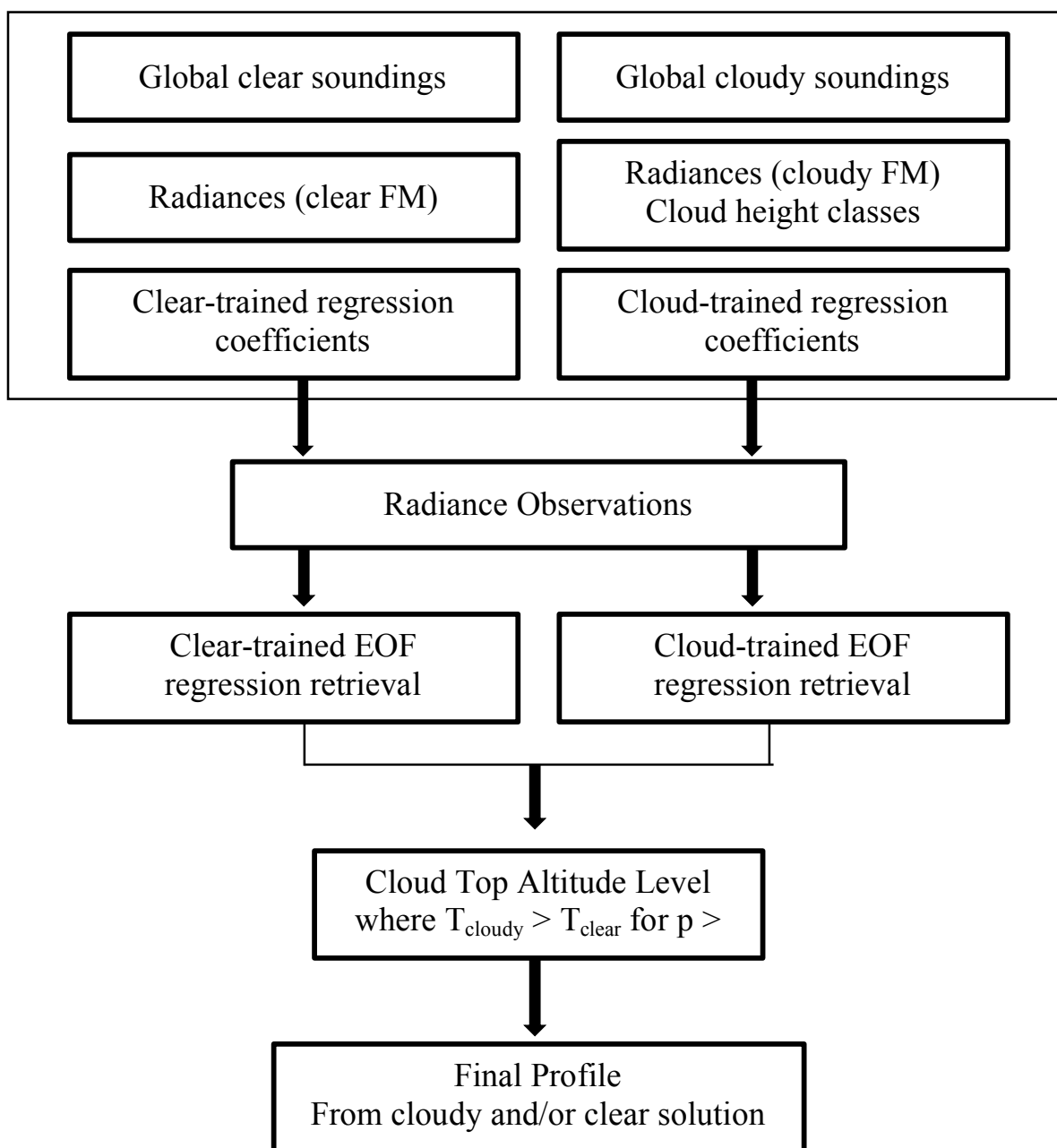


**Figure 4:** Dual Regression retrieval algorithm schematic diagram. Adapted from Figure 1 of Weisz (2015b). “FM” refers to the “forward model” used for radiative transfer calculations.

suite only. Thus, NUCAPS as a proprietary algorithm has the capability to process multiple instruments, but the version available to the user community can only be used with measurements from the Suomi-NPP satellite.

Gambacorta (2012) calls NUCAPS an “iterative regularized least squares minimization algorithm,” noting that the retrieval scheme includes the following steps:

- “(1) A microwave retrieval module which derives cloud liquid water flags and microwave surface emissivity uncertainty;
- (2) A fast eigenvector regression retrieval for temperature and moisture that is trained against ECMWF analysis and CrIS all-sky radiances;
- (3) A cloud clearing module that combines a set of microwave and IR channels (along with, in the future, visible observations provided by the onboard VIIRS instrument);
- (4) A second fast eigenvector regression retrieval for temperature and moisture that is trained against ECMWF analysis and CrIS cloud cleared radiances;
- (5) The final physical retrieval which employs the previous regression retrieval as a first guess.”

Thus, the final IR retrieval module involved in NUCAPS is “an iterated regularized least squared minimization performed on a selected subset of infrared channels” (Gambacorta, 2012). This channel selection is a physically-based process where channels are selected based entirely on their spectral characteristics: high priority is given to “spectral purity, avoidance of redundancy, vertical sensitivity properties, low instrumental noise, and global optimality.” This selection incorporates a sampling of the entire 1305 channels of the CrIS instrument without including them all; Gambacorta (2012) claims that this selection “is capable of reducing significantly the execution time of routine operations, while still

retaining the bulk of the atmospheric variability contained in the original 1305 channel spectrum.”

Radiative transfer calculations are embedded in the NUCAPS retrieval algorithm during the least square residual minimization process. These calculations involve the mean of the microwave Massachusetts Institute of Technology (MIT) microwave and infrared Stand Alone Radiative Transfer Model (SARTA) forward models, and occur at every FOV (Gambacorta, 2012). Brightness temperature tuning, the process of identifying and removing modeling and calibration errors, is a fundamental part of achieving retrieval accuracy as it removes artificial systematic biases. The retrieval output of the NUCAPS algorithm consists of cloud-cleared radiances, surface emissivity and temperature, and vertical profiles of temperature, water vapor, and trace gases.

The NUCAPS retrieval method uses a 3x3 FOV array for its retrieval field. Additionally, the spatial resolution of NUCAPS is roughly 50 km, compromised as a result of incorporating microwave data from the microwave sounders ATMS (Suomi-NPP) and AMSU (Aqua). However, this incorporation of microwave data into the NUCAPS algorithm allows for better retrieval yield below cloudy conditions. Additionally, the inclusion of physical optimal estimation allows for refined sounding profiles in the planetary boundary layer (Weisz, 2015b). A schematic diagram adapted from the NUCAPS Algorithm Theoretical Basis Document (ATBD) of the NUCAPS retrieval algorithm is shown on Fig. 5.

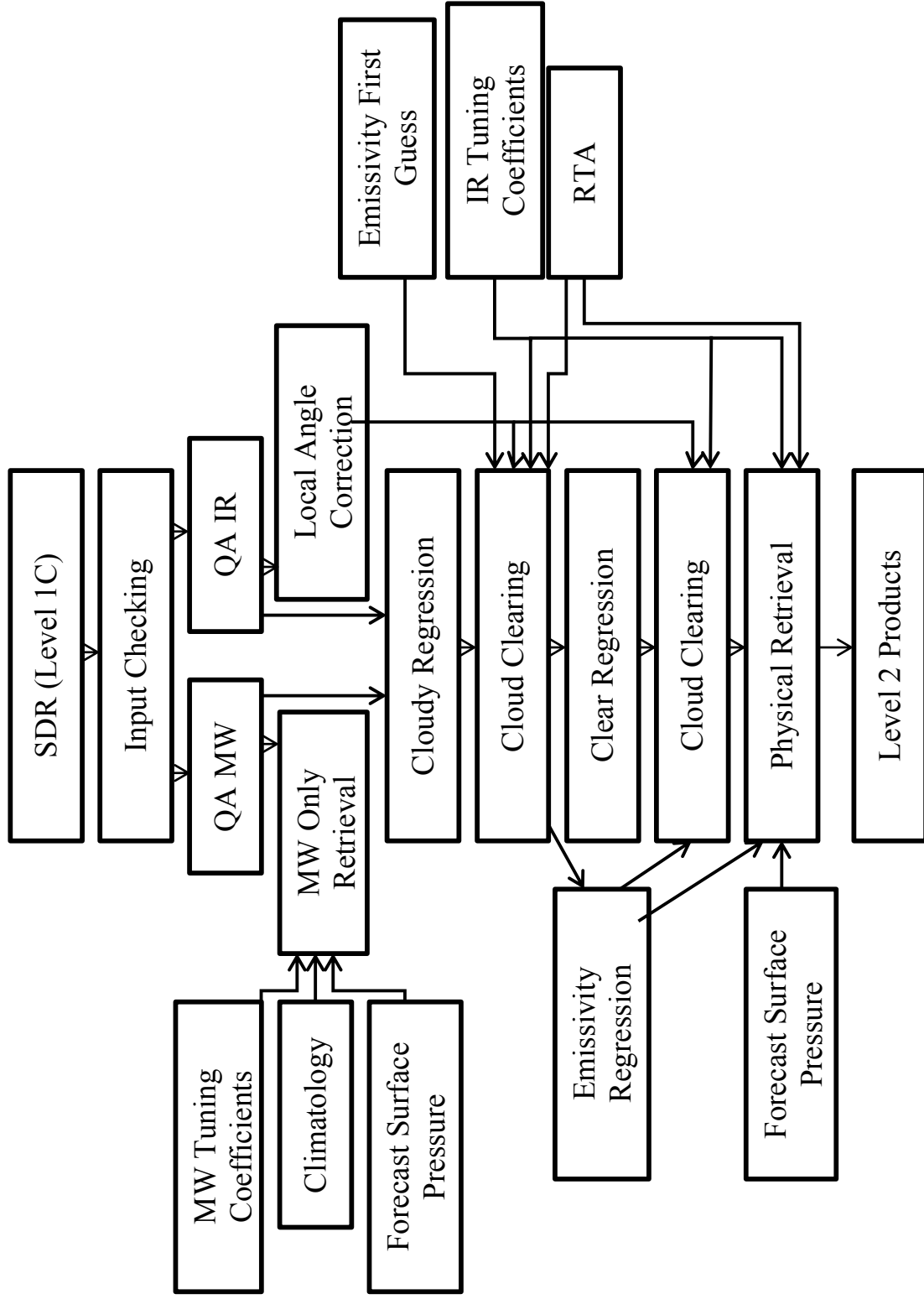


**Figure 5:** NUCAPS retrieval algorithm schematic diagram. Adapted from NUCAPS ATBD.

### 3.3.3 AIRS L2 Standard Physical Retrieval

The AIRS L2 Standard Physical Retrieval algorithm was developed in the early 2000s to support the retrieval of temperature and moisture profiles from the AIRS/AMSU instrument suite. The operational AIRS L2 software is not publicly available through CIMSS CSPP, and thus cannot be independently installed and run by an individual like DR and NUCAPS. The AIRS L2 Standard Physical Retrieval output files are available through download at NASA Goddard Earth Sciences (GES) Data and Information Services Center (DISC)<sup>7</sup>. The AIRS L2 products featured in this study were obtained in this manner.

Linear regression serves as the mathematical basis for the AIRS L2 algorithm. For AIRS L2, this technique includes (1) principal component analysis for data compression, quality control, noise filtering and noise estimation, and regression and (2) AIRS FOV clear detection (Goldberg, 2003). The principal component regression technique provides a very computationally efficient retrieval of atmospheric temperature, moisture, and ozone, as well as surface parameters, such as skin temperature and emissivity. The regression retrieval, often referred to as the initial retrieval, is used as the first guess in the AIRS physical retrieval, and principal component scores are used to select a number of appropriately representative channels without adding the computational burden of using all 2378 AIRS channels.

The AIRS L2 Standard Physical Retrieval algorithm also uses a 3x3 FOV array as its retrieval field, much like NUCAPS. Also much like NUCAPS, the incorporation of microwave data from AMSU compromises its spatial resolution, reducing to roughly 50 km. However, this incorporation of microwave data increases the yield of the retrieval data below

---

<sup>7</sup> NASA GES DISC. <http://disc.gsfc.nasa.gov>.

cloudy conditions. A schematic diagram taken from the AIRS L2 Algorithm Theoretical Basis Document (ATBD) of the AIRS L2 Standard Physical Retrieval algorithm is shown on Fig. 6.

These three retrieval algorithms presented in this study each feature their own unique estimated solution of the vertical profile of the atmosphere at a given time and location, differing particularly in spatial resolution and in the handling of cloudy-sky conditions. The goal of this study is not to argue the superiority of one retrieval algorithm over another, or to validate one retrieval product against another. Rather, the intent of using these three separate retrieval algorithms is to provide comparative solutions of temperature and moisture profiles, and to demonstrate the benefits of each particular algorithm design. Dual Regression data is used for the Yarnell case study, while DR, NUCAPS, and AIRS L2 data are used in the Fort McMurray case study.

### **3.4 Weather Research and Forecasting (WRF) Model**

The Weather Research and Forecasting (WRF) modeling system was developed with the intent to “provide a next-generation mesoscale forecast model and data assimilation system that will advance both the understanding and prediction of mesoscale weather and accelerate the transfer of research advances into operations” (Skamarock, 2005). The model was developed as a collaborative effort among the following agencies: the National Science Foundation (NSF) funded National Center for Atmospheric Research (NCAR) Mesoscale and Microscale Meteorology (MMM) Division; National Oceanic and Atmospheric Administration (NOAA) National Centers for Environmental Prediction (NCEP) and

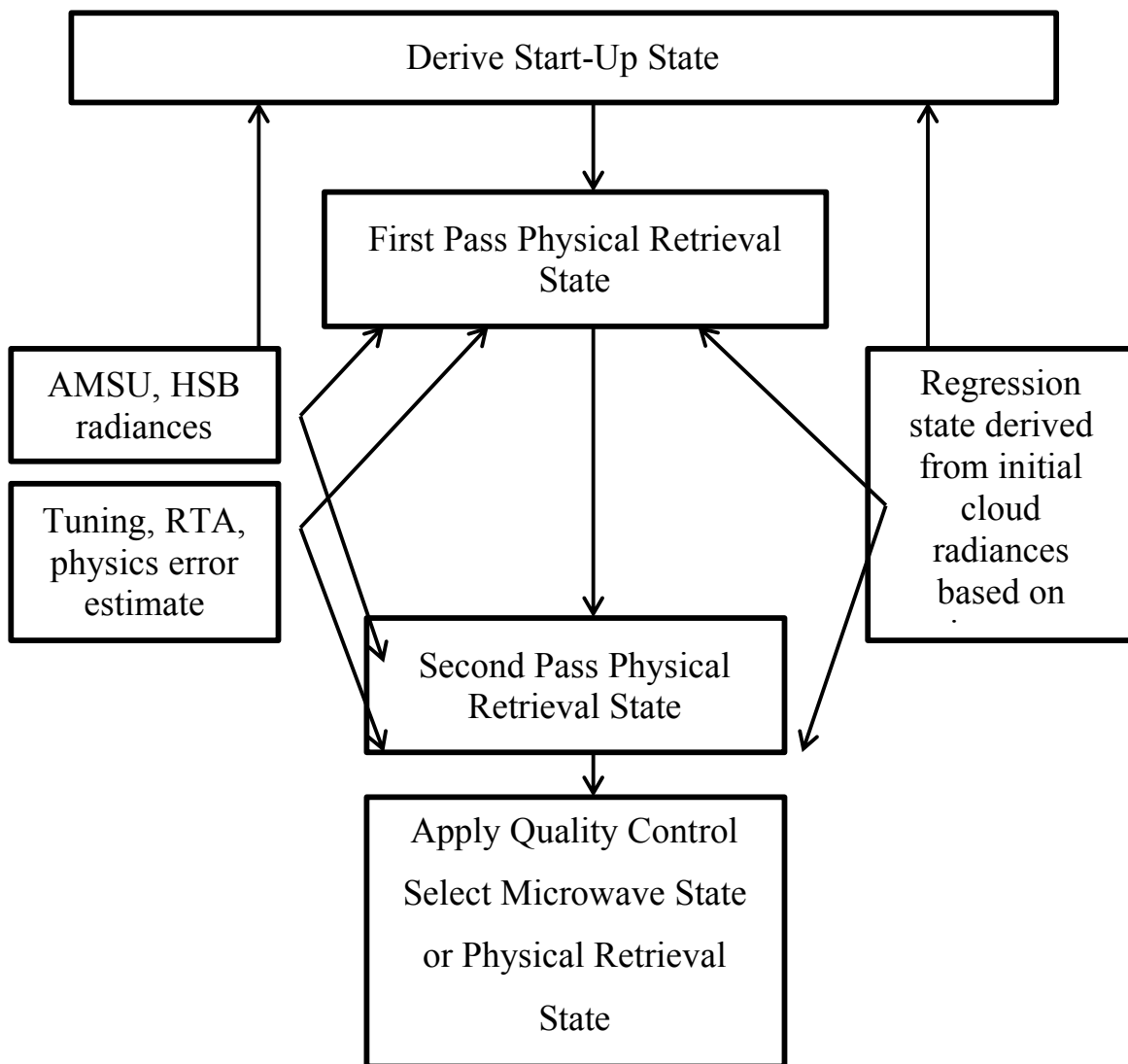


**Figure 6:** AIRS L2 Standard Physical Retrieval algorithm schematic diagram. Adapted from AIRS L2 ATBD.

<b>Algorithm</b>	<b>Dual-Regression (DR)</b>	<b>NUCAPS</b>	<b>AIRS L2</b>
Development	UW/CIMSS	NOAA	NASA
Instrument Capability	AIRS, IASI, CrIS	CrIS	AIRS
Algorithm Basis	Regression	Physical Optimal Estimation	Regression
Radiation Type (Microwave Instrument)	Infrared only	Infrared and Microwave (ATMS)	Infrared and Microwave (AMSU)
Cloud Capability	No retrieval below optically thick cloud	Retrieval below cloud	Retrievals below clouds
FOV Type (Approximate Resolution)	Single FOV resolution (~14 km/nadir)	3x3 FOV Array (~50 km/nadir)	3x3 FOV Array (~40.5 km/nadir)
Design Intent	Research	Operational	Operational

**Table 2:** Specifications of retrieval algorithms DR, NUCAPS, and AIRS L2.

Forecast System Laboratory (FSL); the Department of Defense (DoD) Air Force Weather Agency (AFWA) and Naval Research Laboratory (NRL); the Center for Analysis and Prediction of Storms (CAPS) at the University of Oklahoma; and the Federal Aviation Administration (FAA). Additionally, a number of university scientists contributed to the development as well. The WRF model was designed to be “a flexible, state-of-the-art, portable code that is efficient in a massively parallel computing environment” (Skamarock, 2005). The WRF model is suitable for use in a wide variety of disciplines, including research and operational numerical weather prediction (NWP), data assimilation and parameterized physics research, downscaling climate simulations, air quality research, atmosphere-ocean interaction, and idealized simulations.

The governing equations embedded within the WRF model are formulated using a terrain-following hydrostatic-pressure vertical coordinate system (Skamarock, 2005). For applications of atmospheric radiation, the radiation schemes within the model provide atmospheric heating due to radiative flux divergence and surface downward longwave and shortwave radiation for the ground heat budget. These schemes are one-dimensional, or “column” schemes, with each column treated independently. This is an important part in ensuring accurate vertical thickness of model layers, as the radiative fluxes correspond to those in infinite horizontally uniform planes. These radiation schemes are kept constant, rather than called at every time step, for computational speed and efficiency. The radiation scheme used for this study is the Rapid Radiative Transfer Model (RRTM) Longwave, which is taken from MM5 and uses pre-set tables to accurately represent longwave radiation

processes due to water vapor, ozone, carbon dioxide, and trace gases, as well as accounting for cloud optical depth (Skamarock, 2005).

The WRF model uses a third-order Runge-Kutta scheme for temporal discretization. Additionally, the WRF includes various options for physics packages, cumulus parameterizations, planetary boundary layer schemes, convection schemes, and land-surface models. Embedded in the model are also methods of handling diabatic forcing, hydrostatic balance, Coriolis and curvature terms, advection, and moisture; while these are all crucial parameters in the successful completion of a forecast model, each are far too intricate to address in detail for the scope of this paper. In the case of interest, a full, detailed explanation of the complex, inner workings of the model can be found online<sup>8</sup>.

For the use of WRF data in this study, Version 3.9 of the WRF was compiled and run using six-hour analyses supplemented by three-hour forecasts between analysis times for the case study of the Fort McMurray wildfire, presented in Chapter 4. The outer, larger domain was set to a resolution of 30 km, with an inner, nested domain of 10 km. Figure 7 shows this domain configuration as it applies to the Fort McMurray case. Model output was produced every hour for a 24-hour period during the case. Initial and boundary conditions were identified using National Centers for Environmental Prediction (NCEP) Global Data Assimilation System (GDAS) 0.25 Degree Global Tropospheric Analyses and Forecast Grids<sup>9</sup>. The intent of using these WRF model simulations for the Fort McMurray case was to

---

<sup>8</sup> Advanced Research WRF (ARW) User Guide. <http://mmm.ucar.edu/wrf/users>.

<sup>9</sup> National Centers for Environmental Prediction/National Weather Service/NOAA/U.S. Department of Commerce, 2015: NCEP GDAS/FNL 0.25 Degree Global Tropospheric Analyses and Forecast Grids. Research Data Archive at the National Center for Atmospheric Research, Computational and Information Systems Laboratory, Boulder, CO. Available online at <https://doi.org/10.5065/D65Q4T4Z>.

## WPS Domain Configuration

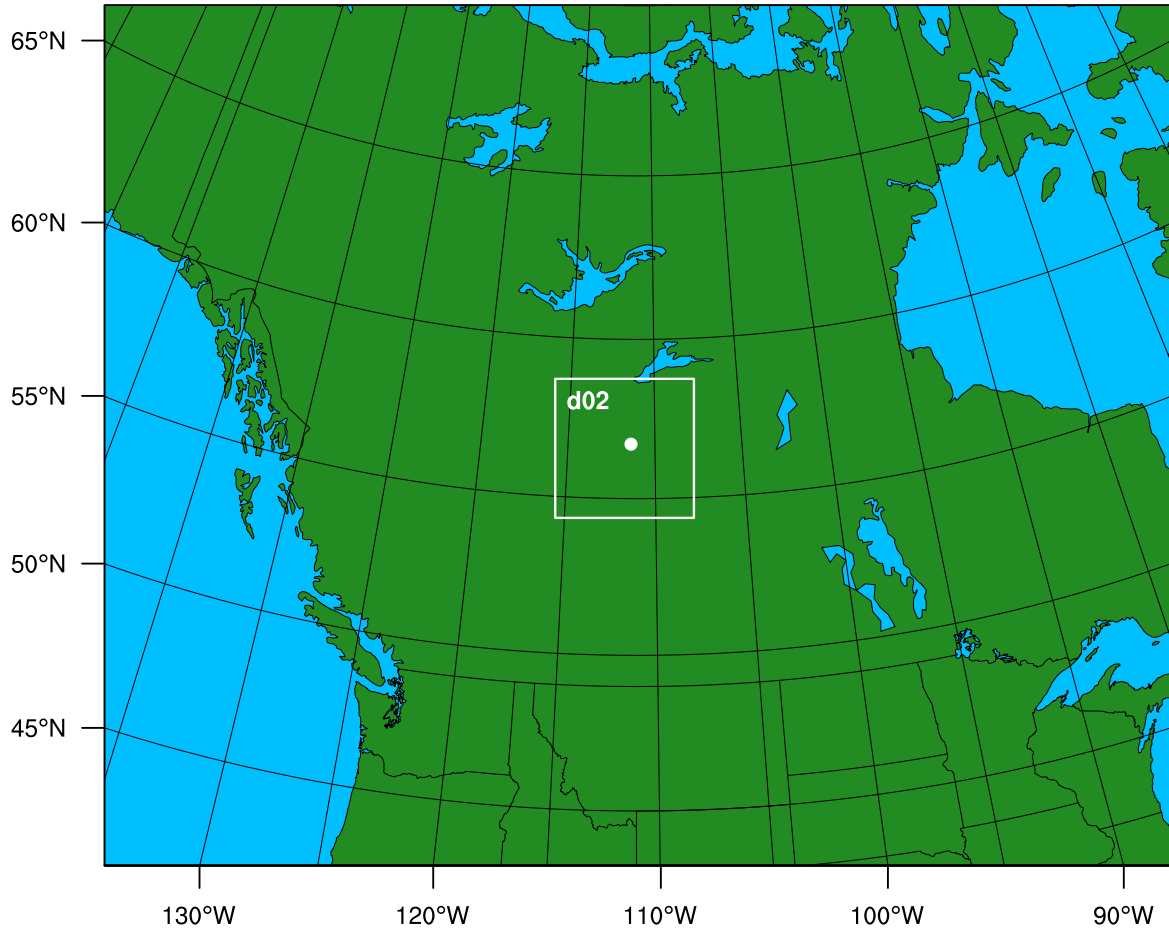


**Figure 7:** Domain configuration in WRF model for Fort McMurray case study. Outer domain denoted by black border. Inner (nested) domain denoted by white border. White dot inside nested domain denotes location of Fort McMurray wildfire.

compare and contrast retrieved profiles to a regional model that provides output at higher temporal resolution relative to that of radiosonde data, thereby correlating closely the timing of the model data with the timing of satellite overpasses.

### 3.5 Additional Data Sources

In addition to Level 1 radiance data from AIRS, IASI, and CrIS, Level 2 retrieval products from Dual Regression, NUCAPS, and AIRS L2, and model output from WRF, various other data sources were incorporated into this study.

Radiosonde profile data for both the Yarnell Hill wildfire case and the Fort McMurray wildfire case were obtained through the University of Wyoming Upper Air Sounding page<sup>10</sup>. Aqua-MODIS True Color images for the Fort McMurray wildfire case were obtained from NASA Goddard Space Flight Center (GSFC) MODIS-Atmosphere<sup>11</sup>. Suomi-NPP True Color images for both the Yarnell Hill wildfire case and the Fort McMurray wildfire case were obtained from NOAA-View Data Exploration Tool<sup>12</sup>. GEFS Reanalysis data were obtained through GEFS Reforecast<sup>13</sup> as GRIB files, and were converted to netCDF files. Output provided from the GEFS Reanalysis data is the control forecast.

---

<sup>10</sup> University of Wyoming Upper Air Soundings.  
<http://weather.uwyo.edu/upperair/sounding.html>.

<sup>11</sup> NASA GSFC MODIS-Atmosphere. <http://modis-atmos.gfsc.nasa.gov>

<sup>12</sup> NOAA-View Data Exploration Tool. <http://www.nnvl.noaa.gov/view/globaldata.html>

<sup>13</sup> GEFS Reforecast Data. <https://www.esrl.noaa.gov/psd/forecasts/reforecast2/>

## **4 Case Studies**

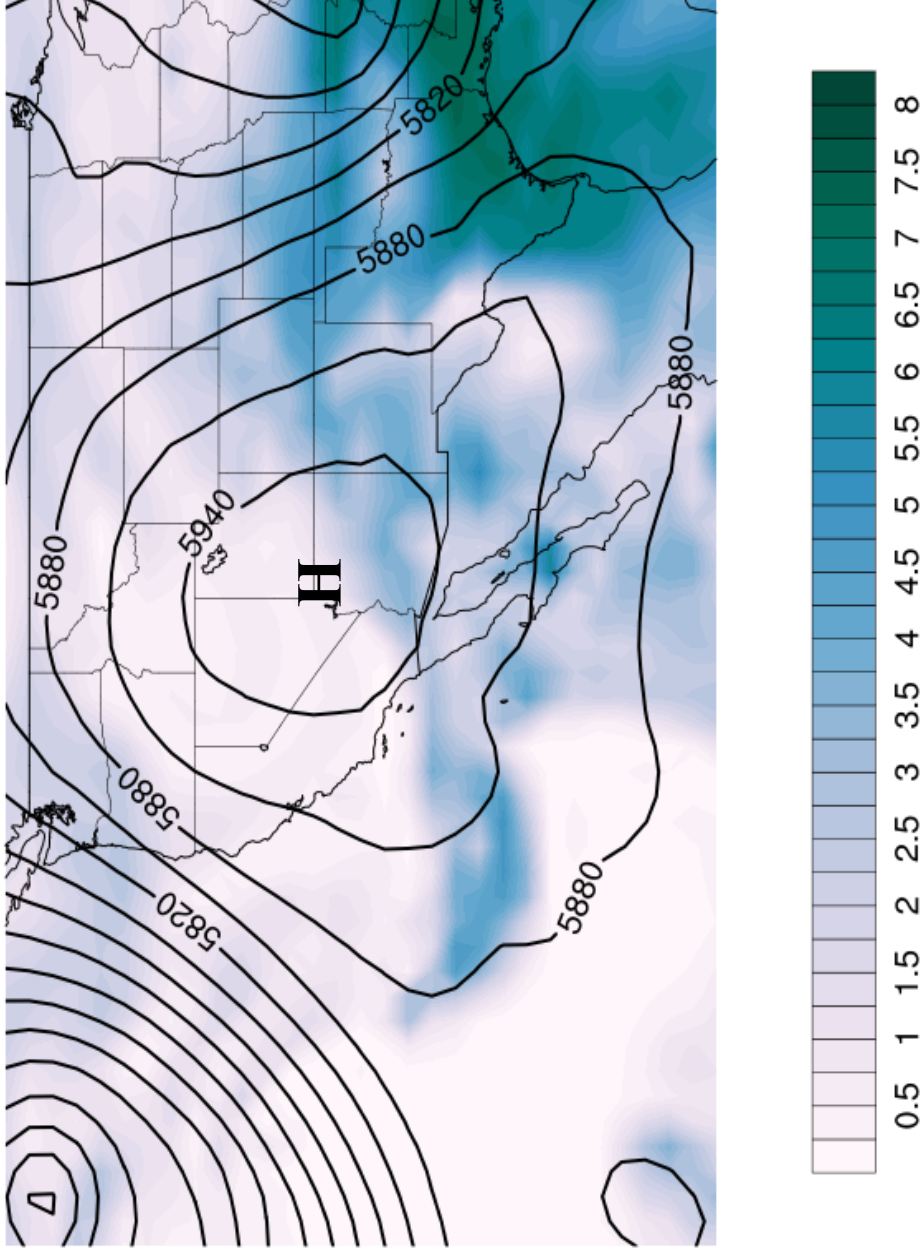
### **4.1 Yarnell Hill Wildfire**

The Yarnell Hill wildfire was ignited by several lightning strikes on 28 June 2013 at approximately 2300 UTC in Yarnell, Arizona. The area had not experienced fire since 1966; thus, the fuel load in the region was dangerously high given drought conditions and exceptionally high temperatures (Hardy, 2014). Fire conditions became more favorable for rapid growth on 30 June, by which time the fire had spread from an initial half-acre in size to 300 acres. PyroCb activity developed that afternoon at approximately 2345 UTC; the overshooting cloud top signature that detected such activity is shown via GOES-15 visible imagery on Fig. 8. A line of thunderstorms moved into the Yarnell area from the northeast as a prelude to the overshooting top signature. A convective outflow boundary is suspected to have caused rapid intensification of the fire and an abrupt change in wind direction; the sudden change in conditions tragically killed nineteen members of the Granite Mountain Interagency Hotshot Crew as they attempted to shelter in place (Bachmeier, 2013; Hardy, 2014).

The synoptic setup of the Yarnell Hill wildfire prescribes to the “monsoonal anticyclone” classification scheme of Dr. David Peterson. Figure 9 shows GEFS Reanalysis data for 30 June 2013 at 1800 UTC. The strong ridge in 500 hPa geopotential height and associated mid-tropospheric anticyclone was centered over the southwestern United States. The associated anticyclonic flow around this anticyclone allowed for the advection of moisture from the Four Corners region into central Arizona, providing a mechanism for the development of traditional convection over the high terrain of the Yarnell Hill wildfire



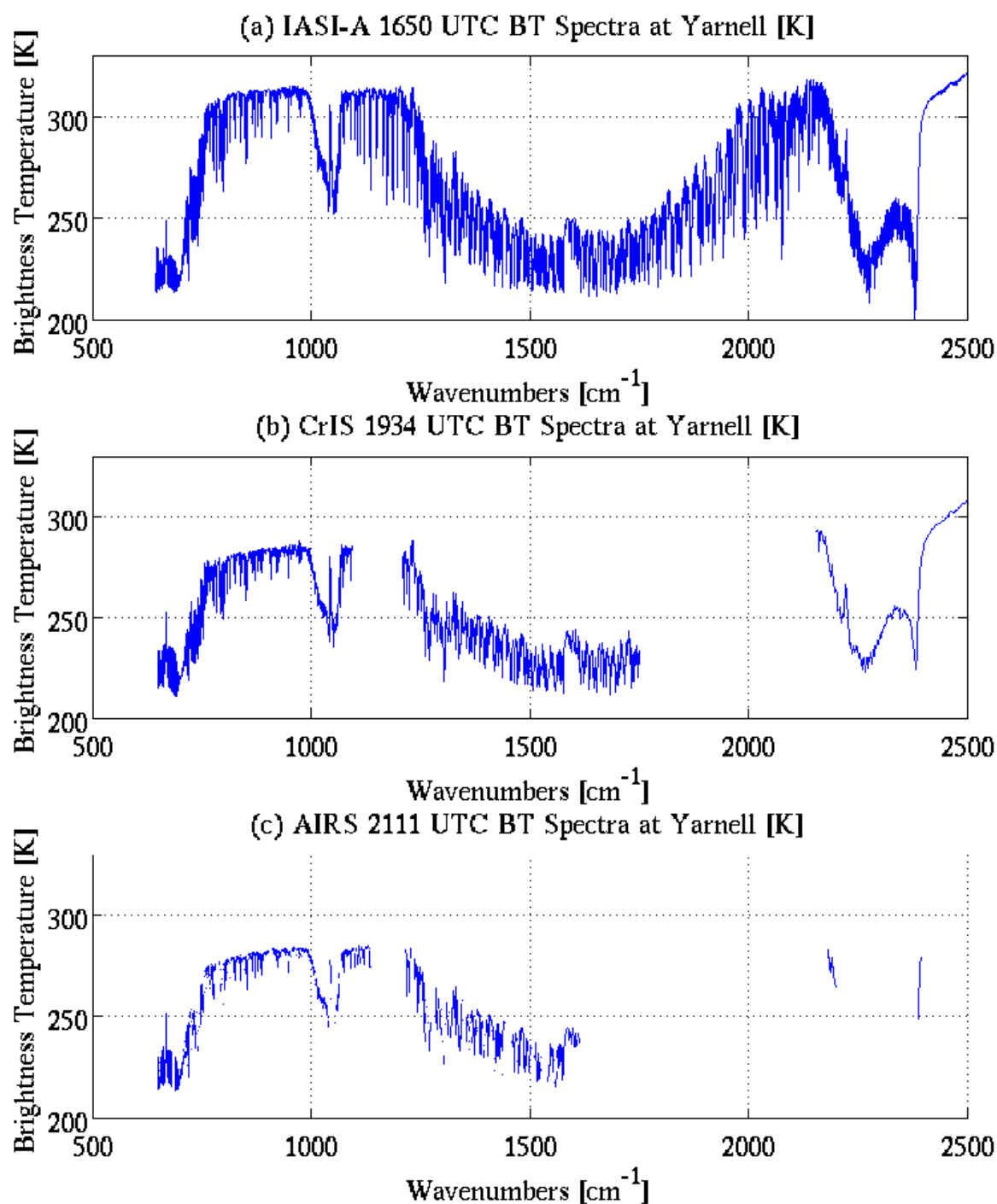
500 hPa Geopotential Heights and Specific Humidity, 2013 June 30 1800 UTC (m) ( $\text{g kg}^{-1}$ )



**Figure 9:** GFS Reanalysis data for Yarnell Hill wildfire, 30 June 2013, at 1800 UTC. Black contours indicate 500-hPa geopotential heights in meters, contoured in 30-m intervals. Shading indicates 500-hPa specific humidity in grams per kilogram, in 0.25- $\text{g kg}^{-1}$  intervals.

sufficient enough for PyroCb development (Peterson, 2017b). The spatial distribution of mid-tropospheric moisture across the southwestern United States, shown on Fig. 9, demonstrates the setup for moisture advection with a northeasterly anticyclonic flow of higher moisture content into the Yarnell area.

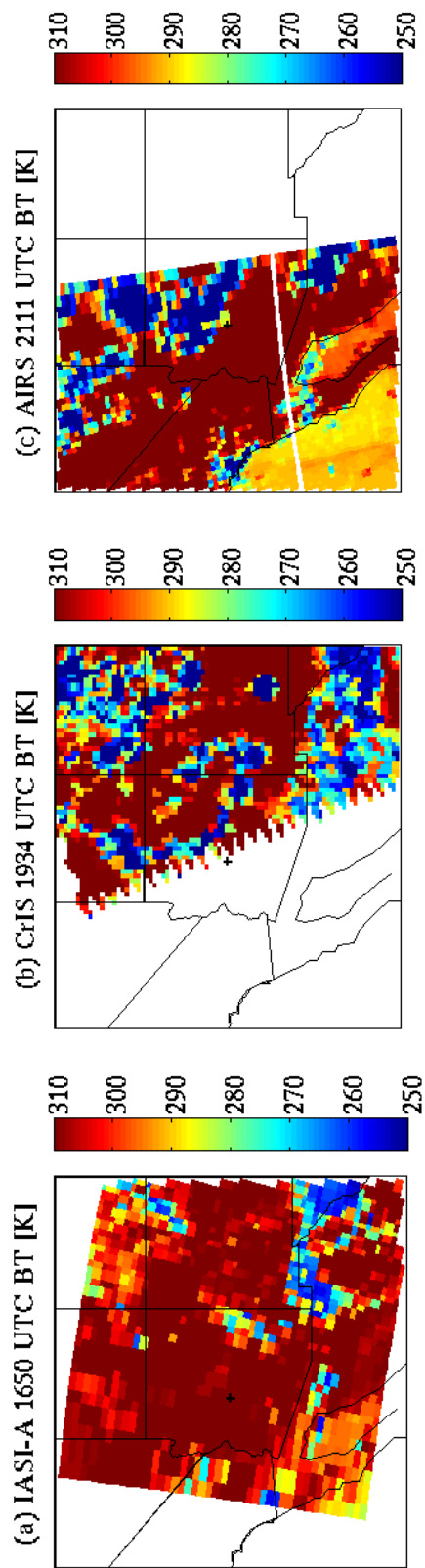
Level 1 data for the afternoon overpasses of 30 June indicate warm surface temperatures and support the existence of the incoming convective system from the northeast observed by visible imagery. Figure 10 shows spectra of observed brightness temperatures from the location of the Yarnell Hill wildfire, representing successive satellite overpasses on the afternoon of 30 June at (a) 1650 UTC, (b) 1934 UTC, and (c) 2111 UTC. IASI-A, shown in (a), overpassed Yarnell at 1650 UTC and observed very warm temperatures surpassing 320 K within the window region. CrIS, shown in (b), overpassed the Arizona and New Mexico region at 1934 UTC, roughly three hours after IASI-A. However, the satellite did not pass over the exact location of the Yarnell Hill wildfire, passing slightly to the east; thus, the spectrum shown in (b) is taken from the location closest to Yarnell within the granule. In (b), cooler temperatures are observed in the window region, indicative of cloudy-sky conditions over the area at that time. AIRS, shown in (c), overpassed Yarnell at 2111 UTC, almost two hours after CrIS, and observed relatively similar cooler temperatures in the window region, implying that cloudy-sky conditions existed again over Yarnell at that time. It is worth noting that at 2111 UTC, this overpass from AIRS provided the closest hyperspectral measurements in time to the PyroCb activity observed at 2345 UTC, but a temporal separation of two and a half hours between the overpass and the PyroCb is not ideal, especially when investigating an event on such small scales of time and space.



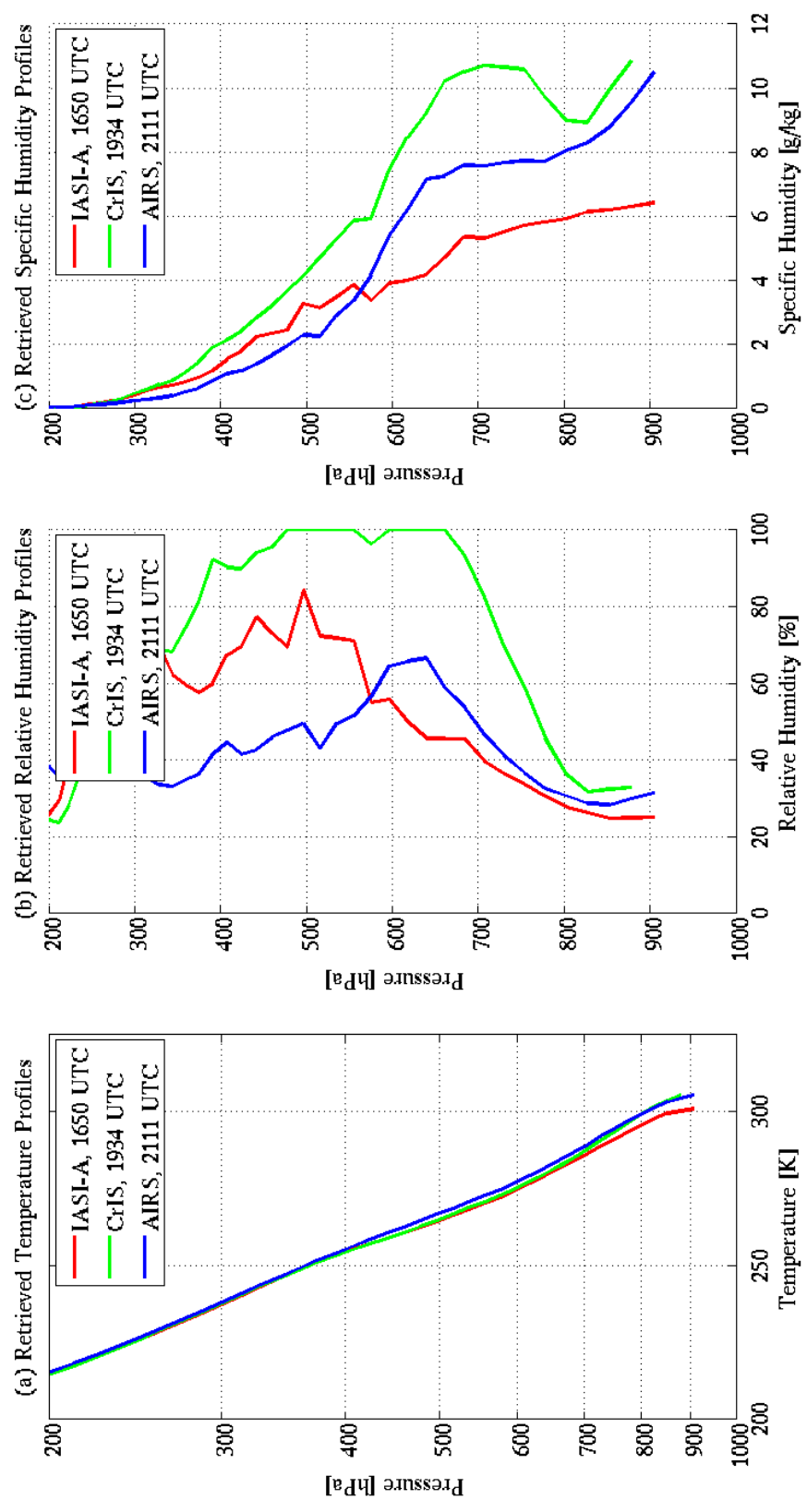
**Figure 10:** Observed brightness temperature spectra for Yarnell Hill wildfire location, 30 June 2013, for (a) IASI-A at 1650 UTC; (b) CrIS at 1934 UTC; and (c) AIRS at 2111 UTC.

Figure 11 shows observed brightness temperatures at 10.9  $\mu\text{m}$  for each of the successive afternoon overpasses of the three hyperspectral sounders. The aforementioned warm temperatures within the window region of the spectrum observed by IASI-A are supported by temperatures surpassing 310 K in much of central and northern Arizona, as shown in (a). These warm brightness temperatures suggest extremely warm surface temperatures, as the cloud-free atmospheric column allows the atmosphere to act more like a blackbody, and therefore brightness temperatures are an appropriate representation of surface temperatures. At the time of the IASI-A overpass, 1650 UTC, the incoming convective system was not yet observed to the northeast of Yarnell. The location of Yarnell just outside the CrIS overpass is evident in (b), but the eastward path of the granule is still beneficial as it depicts cold brightness temperatures northeast of Yarnell, indicating the development of the incoming convective system. It is important to note that the brightness temperatures observed by CrIS in (b) have been interpolated to a uniform 15-km grid; this was done to smooth the edges of the granule and preserve information that is lost at the outermost edges due to the high-scanning angle of the instrument. The AIRS overpass at 2111 UTC, shown in (c), most strongly confirms the incoming line of thunderstorms to the northeast, as indicated by the leading edge of cold temperatures below 250 K approaching the Yarnell area. The formation of this feature also closely matches the shape of the system observed via satellite imagery.

Figure 12 shows retrieved vertical profiles of temperature, (a), relative humidity (RH), (b), and specific humidity, (c), for the afternoon overpasses of each instrument on 30 June at the exact location of the Yarnell wildfire. These profiles were all retrieved using the



**Figure 11:** Brightness temperature observations at  $10.9 \mu\text{m}$  on 30 June 2013, across the southwestern United States, by (a) IASI-A at 1650 UTC; (b) CrIS at 1934 UTC; and (c) AIRS at 2111 UTC. Data in (b) interpolated to uniform 15-km grid. Location of Yarnell Hill wildfire denoted by a black plus sign.



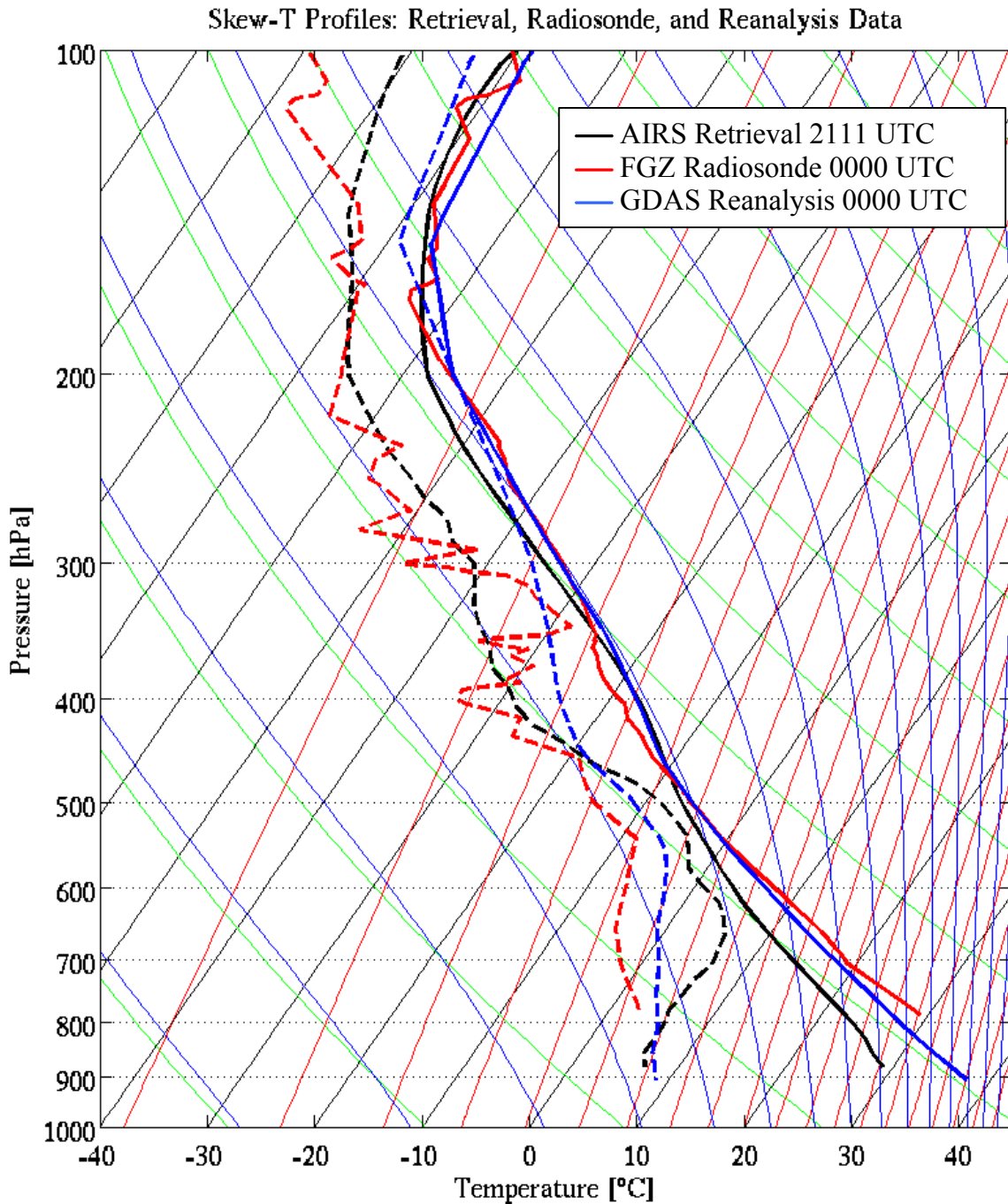
**Figure 12:** Vertical profiles of (a) temperature, (b) relative humidity, and (c) specific humidity for each instrument during afternoon overpasses on 30 June 2013. Profiles retrieved using the Dual Regression retrieval algorithm.

Dual Regression algorithm; doing so allows for direct comparison between the overpasses as spatial and vertical resolutions and parameter calculations are identical for each profile.

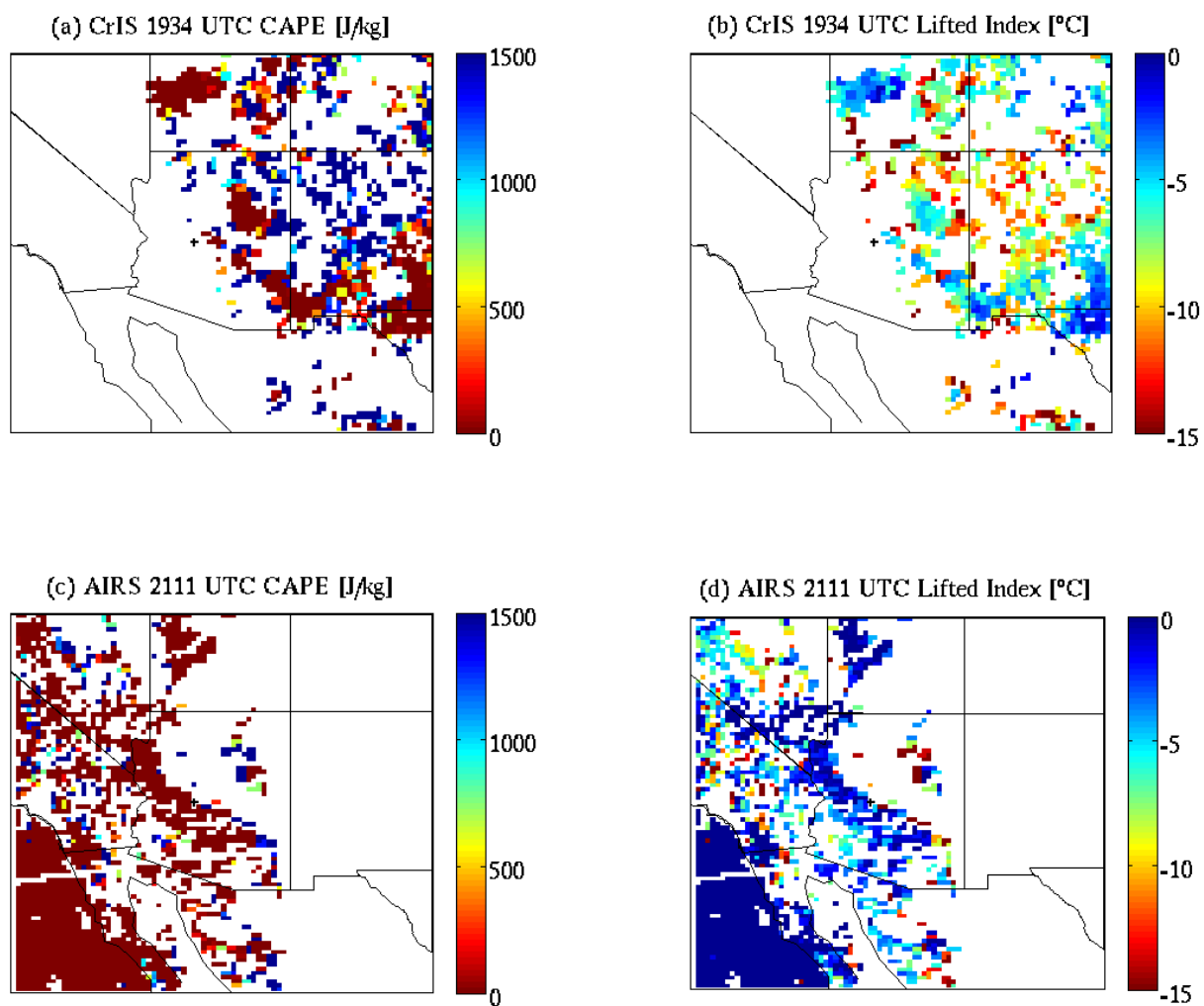
The temperature profiles between the three overpasses are relatively consistent through much of the vertical column, with increasing surface temperatures between the earliest IASI-A overpass and the AIRS overpass nearly five hours later. The relative humidity profiles differ significantly throughout the column, however. Surface values of relative humidity increase from roughly 25% at 1650 UTC to near 35% at 1934 UTC and 2111 UTC. The profiles diverge from one another significantly in the middle troposphere, where values of 45-50% are observed at 1650 UTC and at 2111 UTC near 700-hPa, but values approaching 100% are observed in between these two time periods at 1934 UTC. This could possibly be a result of clouds within the atmospheric column, as the brightness temperature spectra showed cooler temperatures within the window region, thus suggesting cloudy conditions over Yarnell during this overpass. While these three relative humidity profiles are indeed distinct, it is worth noting that each has a relative maximum between 750 – 500-hPa. Specific humidity profiles exhibit similar behavior throughout the atmospheric column, with the most moisture observed at the middle time-step of 1934 UTC. Surface values of specific humidity increase dramatically between the first overpass and the later two, increasing from roughly 6 g/kg at 1650 UTC to near 11 g/kg at 1934 UTC and 2111 UTC. There also exists a pocket of moisture in the CrIS and AIRS overpasses between 750 – 500-hPa, in the same region of the column where all three relative humidity profiles reached their peaks. This mid-level moisture signature is intriguing, as Peterson (2015) had previously found ambient mid-level moisture to be a potentially key ingredient to PyroCb development.

Figure 13 shows the latest afternoon overpass of AIRS at 2111 UTC compared to radiosonde and reanalysis data on a Skew-T diagram, and clearly demonstrates the importance in noting differences in time and space when making such a comparison. The 2111 UTC overpass of AIRS is roughly three hours ahead of both the Flagstaff radiosonde and the GDAS reanalysis data, both of which are valid at 0000 UTC on 01 July. Additionally, while the GDAS and AIRS profiles are collocated well nearest the Yarnell wildfire, the Flagstaff radiosonde is roughly 125 miles to the northeast. As no two share the same temporal or spatial characteristics, the comparison between the three overpasses and the radiosonde is unfavorable. This “best-available” comparison shows relatively similar temperature structures throughout the troposphere, however, with the exception of slight divergence between all three at the surface. The GDAS and radiosonde profiles are much warmer at the surface than that of AIRS, likely due to the three-hour time difference. Additionally, the three dew-point temperature profiles are seemingly in disagreement throughout the entire atmospheric column, with the GDAS profile showing a significantly moist profile from roughly 600-hPa upward that the radiosonde and retrieval both do not feature.

Figure 14 shows two different parameters used for measuring the instability of the environment: Convective Available Potential Energy (CAPE) and Lifted Index (LI) derived from hyperspectral retrievals. High values of CAPE and low, negative values of LI both denote an unstable environment conducive for convective development. All four plots in Figure 14 feature data interpolated to a uniform 15-km grid. While the exact location of the Yarnell fire (denoted by the black plus sign) is not retrieved for either the CrIS overpass at 1934 UTC or the AIRS overpass at 2111 UTC, it proves useful to observe the stability of the



**Figure 13:** Skew-T diagram with solid lines indicating temperature (in Celsius) and dashed lines indicating dew-point temperature (in Celsius). Black profiles denote AIRS retrieval from 2111 UTC 30 June 2013. Red profiles denote Flagstaff, Arizona radiosonde from 0000 UTC 01 July 2013. Blue profiles denote GDAS reanalysis at Yarnell from 0000 UTC 01 July 2013.



**Figure 14:** Retrieved values of Convective Available Potential Energy (CAPE) (a,c) and Lifted Index (LI) (b,d) for CrIS and AIRS overpasses at 1934 UTC and 2111 UTC, respectively. Data interpolated to a uniform 15-km grid. Exact location of the Yarnell wildfire is denoted by a black plus sign.

surrounding environment. Values of CAPE exceeding 1500 J/kg and LI values below -15 C existed in the surrounding area of Yarnell during both overpasses. Thus, it can be inferred that the environment preceding the PyroCb event was highly unstable, ripe for convective development.

The use of hyperspectral satellite data in the investigation of the Yarnell Hill wildfire helped show the very warm, dry surface conditions that led to the enhancement of the fire on 30 June. Additionally, hyperspectral brightness temperatures confirmed the development of the incoming convective system from the northeast as seen via visible imagery. Analysis of retrieved profiles over the timespan of the three afternoon overpasses showed increasing heat throughout the afternoon, as well as an increase in mid-level moisture between 750 – 500-hPa. Values of CAPE and LI both show regions of high instability in the environment preceding the PyroCb, as well. However, the timing of the satellite overpasses for this case study were not ideal when comparing with the time of the PyroCb event, as two and a half hours separated the last overpass with the observed PyroCb. Likewise, differences in time and space made comparisons between the overpasses to radiosonde and reanalysis data difficult as well. Nevertheless, the use of hyperspectral data in this case provided a unique glimpse into the environment precluding the PyroCb that traditional in-situ observations would otherwise not provide.

## 4.2 Fort McMurray Wildfire

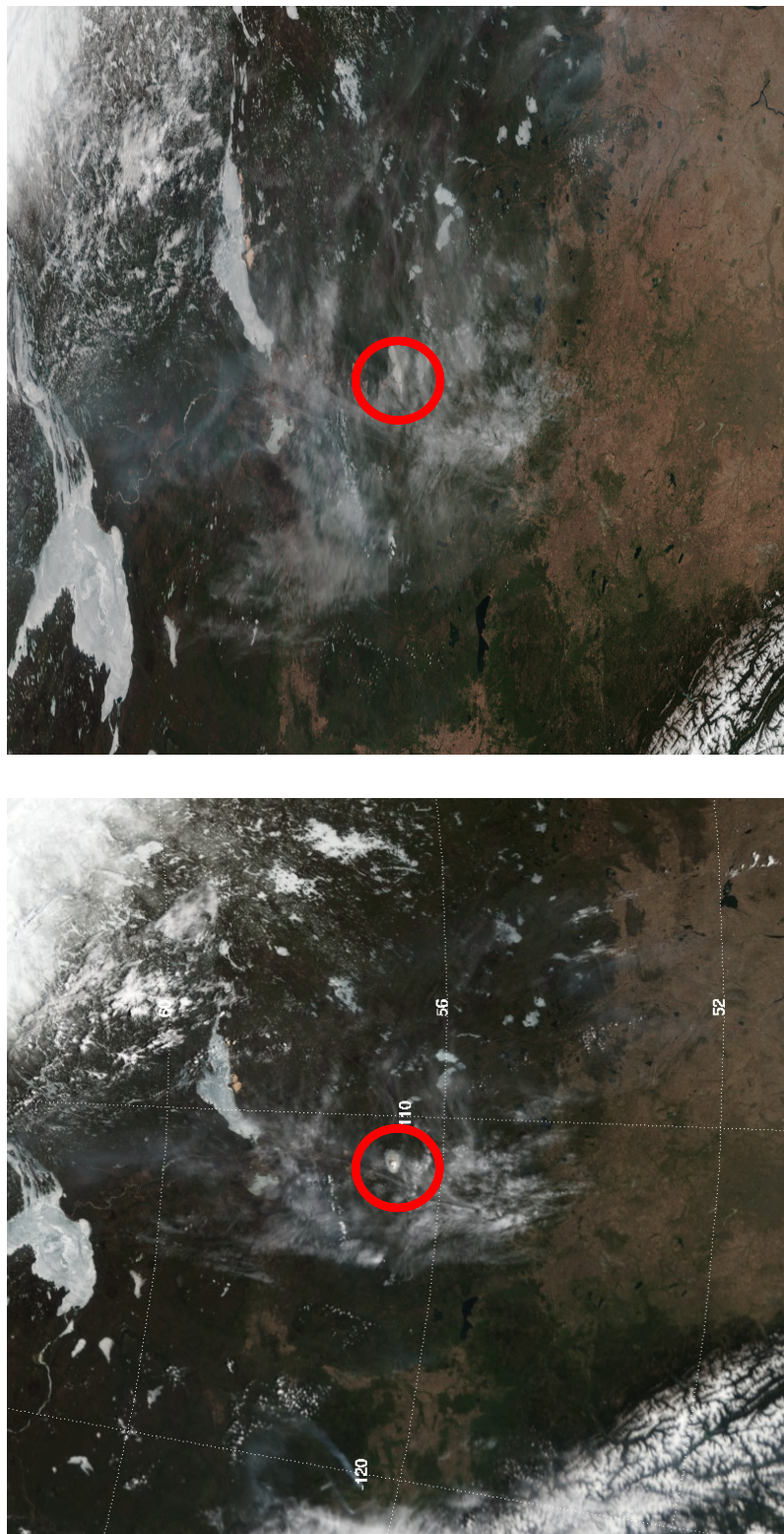
The Fort McMurray wildfire in Fort McMurray, Alberta was chosen as a second case study, largely because its higher latitude meant a higher number of potentially overlapping satellite overpasses. The fire began on 1 May 2016 in the absence of a known cause, and PyroCb development was detected via visible imagery two days later on 03 May. Multiple PyroCb events would later develop, as the Fort McMurray fire would continue to burn for weeks, prompting the largest wildfire evacuation (90,000 residents) in Alberta history<sup>13</sup>. At \$8.9 billion (USD), the fire was also deemed the costliest disaster in Canadian history, with the provincial state of emergency lasting from 4 May to 1 July. The fire was not officially declared “under control” until 5 July.

Figure 15 features the visible images that show the initial PyroCb development on 3 May, with the Aqua satellite overpassing Fort McMurray at 1950 UTC and the Suomi-NPP satellite overpassing at 2022 UTC, nearly one half hour later. Overshooting cloud tops are observed in both images; at 1950 UTC, the plume has a circular shape, but at 2022 UTC, the plume has already been transported to the east while the shape becomes elongated. The detected PyroCb exists within an existing region of clouds, making a potential retrieval using Dual Regression slightly more challenging.

The synoptic setup of the Fort McMurray wildfire does not distinctly fall into the “Canadian Ridge Breakdown” classification scheme of Dr. David Peterson, but there does exist a strong ridge in 500-hPa geopotential heights around western Canada, as shown by Fig. 16. This ridge began to break down on 05 May, perhaps serving as a trigger mechanism for

---

<sup>13</sup> Global News Canada, The Canadian Press. Fort McMurray Wildfire. <http://globalnews.ca/news/3187254/fort-mcmurray-wildfire-study-pegs-cost-of-lost-buildings-income-and-environmental-damage-at-9-5b/>



**Figure 15:** Visible images of Fort McMurray PyroCb event from (a) Aqua MODIS True Color at 1950 UTC 03 May 2016, left; and (b) Suomi-NPP VIIRS True Color at 2022 UTC on 03 May 2016. Red circles indicate location of PyroCb development.

500 hPa Geopotential Heights and Specific Humidity, 2016 May 04 0000 UTC (m) ( $\text{g kg}^{-1}$ )

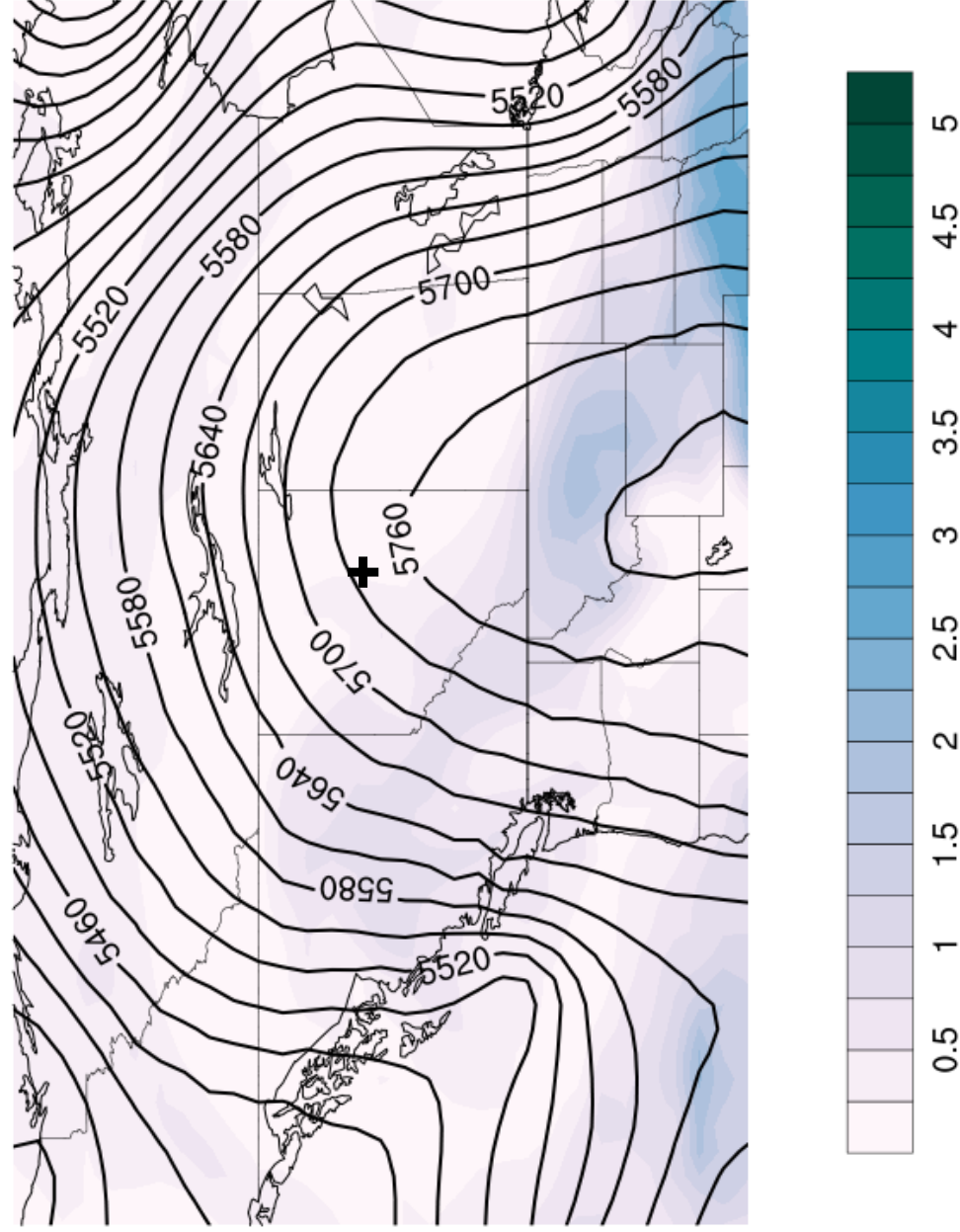


**Figure 16:** GEFS Reanalysis data for Fort McMurray wildfire, 04 May 2016, at 0000 UTC. Black contours indicate 500-hPa geopotential heights in meters, contoured in 30-m intervals. Shading indicates 500-mb specific humidity in grams per kilogram, in 0.25-g/kg intervals.

the development of later PyroCb events observed within this wildfire (Bachmeier, 2016). Also shown on Fig. 16 is a relatively lackluster moisture structure at 500-hPa, suggesting less moisture being advected into the region than was observed with the setup of the Yarnell Hill wildfire. However, further analysis of moisture at various levels of the atmosphere will be presented with retrieved vertical profiles.

Due to the temporal proximity of the Aqua and Suomi-NPP satellite overpasses to one another and to the PyroCb event, AIRS and CrIS data were exclusively used for this study. Figure 17 shows observed brightness temperature spectral for (a) AIRS at 1947 UTC and (b) CrIS at 2018 UTC, with both spectra featuring relatively cold temperatures in the window region. In both spectra, temperatures specifically become colder nearest the absorption band around  $700\text{ cm}^{-1}$ , implying the presence of a high, cold cloud in the atmospheric column. Figure 18 shows observed brightness temperatures at  $910\text{ cm}^{-1}$  for (a) AIRS at 1947 UTC and (b) CrIS at 2018 UTC on 03 May. Recall that the PyroCb event detected by visible imagery in Figure 15 existed in a region of clouds; the cold brightness temperatures between 250 K – 270 K near the Fort McMurray region match the shape of the cloud signatures on visible imagery. At 15-km grid resolution, it is difficult to detect the exact signature of the overshooting top from brightness temperatures alone due to this prevalence of clouds in the region. However, a small but significant feature of extremely cold brightness temperatures (less than 250 K) appears on the CrIS overpass at 2018 UTC that is not observed just thirty minutes prior by AIRS. When combining these observations to the visible images, one can infer that this small feature is related to the development of the PyroCb event.

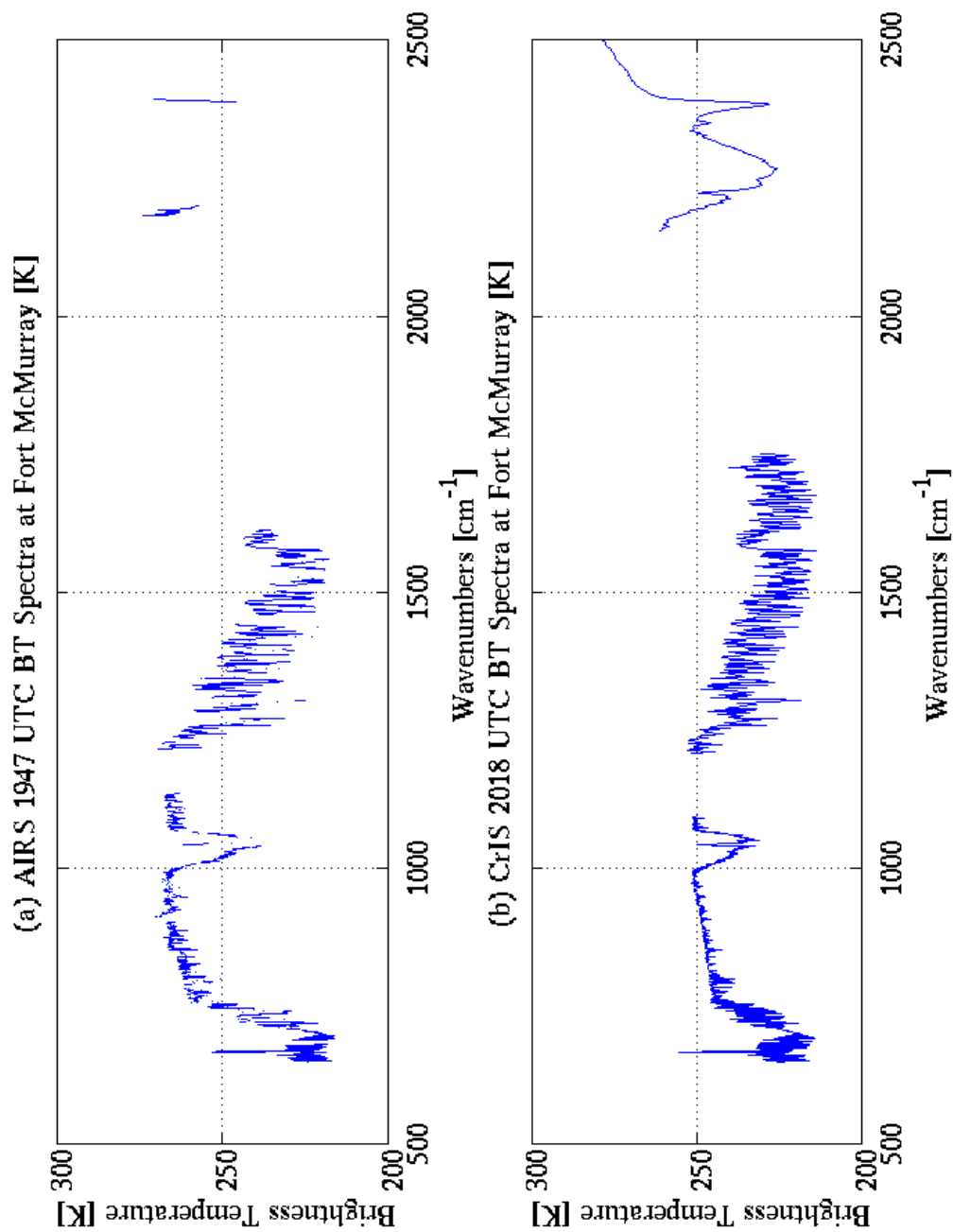
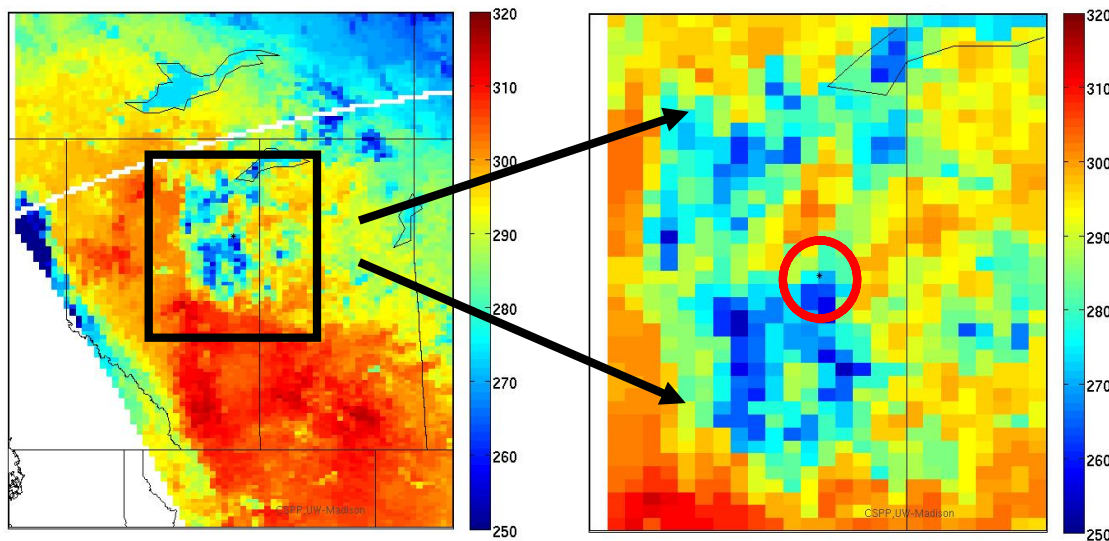


**Figure 17:** Observed brightness temperature spectra at Fort McMurray, 03 May 2016, by (a) AIRS at 1947 UTC and (b) CrIS at 2018 UTC.

(a) AIRS 1947 UTC Brightness Temperatures



(b) CrIS 2018 UTC Brightness Temperatures [K]

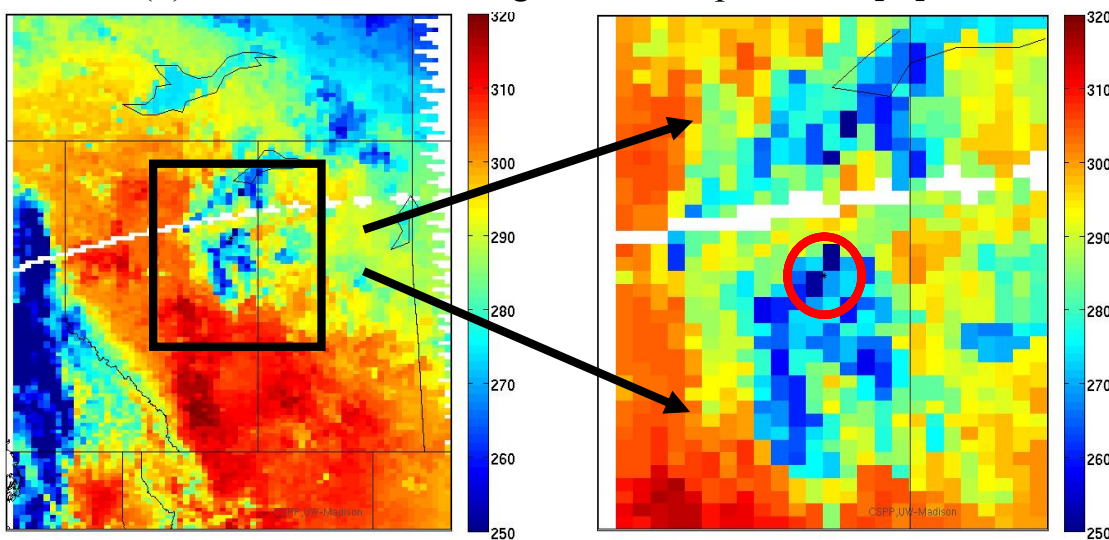
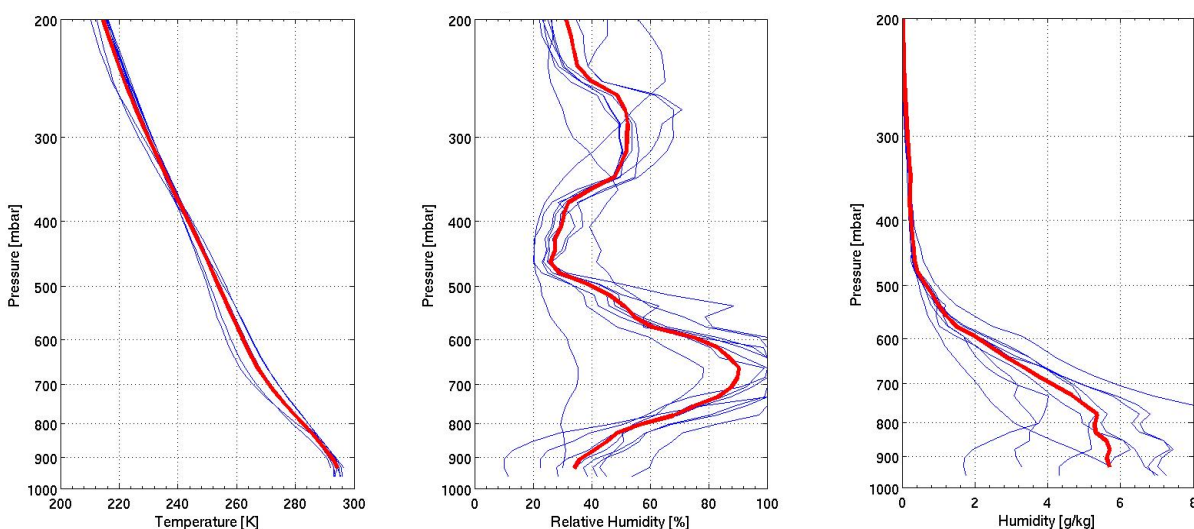


**Figure 18:** Brightness temperature observations at  $10.9 \mu\text{m}$ , 03 May 2016, by (a) AIRS at 1947 UTC and (b) CrIS at 2018 UTC. Data interpolated to uniform 15-km grid. Location of Fort McMurray denoted by red circle. Black box and arrows in left figures denote region of zoom in right figures.

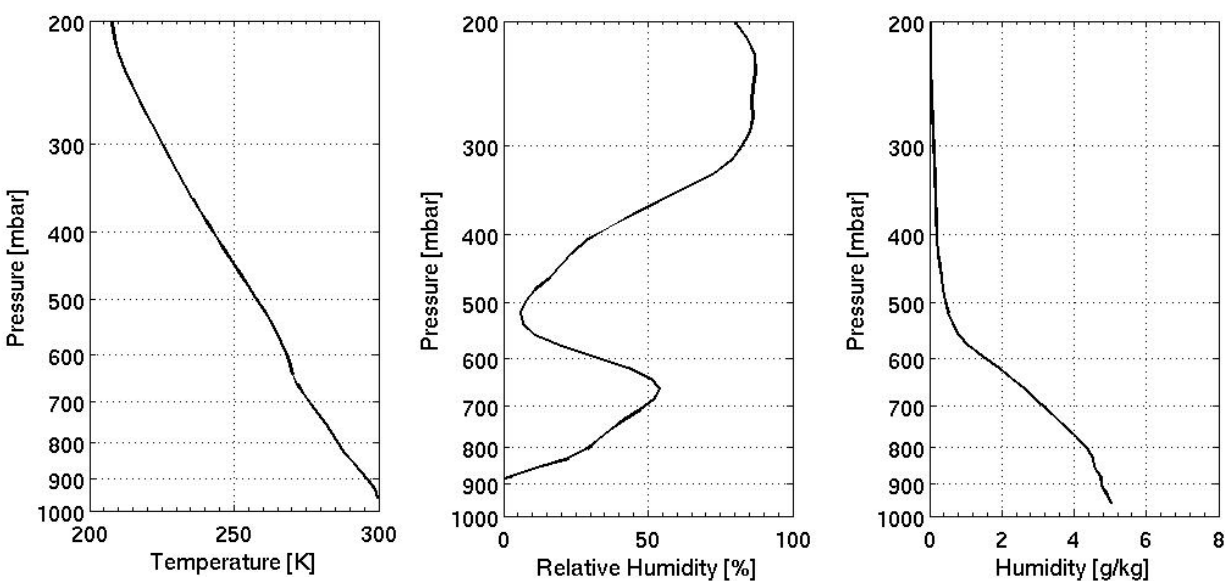
For Level 2 retrieval data, three retrieval algorithms were used in this study: Dual-Regression, NUCAPS, and AIRS L2. Recall that the spatial resolution of DR is roughly 14km, as it uses one single FOV for the area of retrieval, but that the spatial resolutions of both NUCAPS and AIRS L2 are approximately three times coarser as they both use a 3x3 FOV array. Therefore, in order to make an appropriate comparison between the three retrieval algorithms, nine single FOV's centered on Fort McMurray from Dual Regression were averaged. The mean of these nine FOV's then gives a profile representative of the same 3x3 FOV array that is used in NUCAPS and AIRS L2. Thus, comparisons between the algorithms can be made more equally. Fig. 19 (a) shows these nine Dual Regression profiles in blue that were used to calculate the mean profile in red; then, the red profiles can be more accurately compared to the NUCAPS retrievals in (b). Vertical profiles of temperature remain relatively consistent between the two algorithms, with surface temperatures retrieved by NUCAPS being slightly warmer than those by Dual Regression. While relative humidity values are consistently higher in the lower- to mid-troposphere with DR, values are much higher in the UTLS with NUCAPS. Noteworthy, however, is that both relative humidity profiles feature similar structures, with peaks in relative humidity occurring near 700-hPa and relative minimum values occurring near 500-hPa. Interestingly, the specific humidity profiles between the two algorithms are strikingly similar throughout much of the column, with surface values around  $5 \text{ g kg}^{-1}$  and 700-hPa values around  $3.5 \text{ g kg}^{-1}$ . However, DR does show slightly more moisture in the lower troposphere than NUCAPS.

Figure 20 shows retrieved profiles of (a) temperature, (b) relative humidity, and (c) specific humidity. The operational AIRS L2 retrieved profiles are shown in red for the 1947 UTC overpass of AIRS, whereas the NUCAPS retrieved profiles are shown in blue for the

(a) Vertical Profiles from Dual Regression Algorithm



(b) Vertical Profiles from NUCAPS Algorithm



**Figure 19:** Vertical profiles of temperature (left), relative humidity (center), and specific humidity (right) retrieved from CrIS at 2018 UTC 03 May 2016, using (a) the Dual Regression algorithm and (b) the NUCAPS algorithm. Red profiles in (a) represent the mean of the nine profiles in blue, calculated in order to match the resolution in (b).

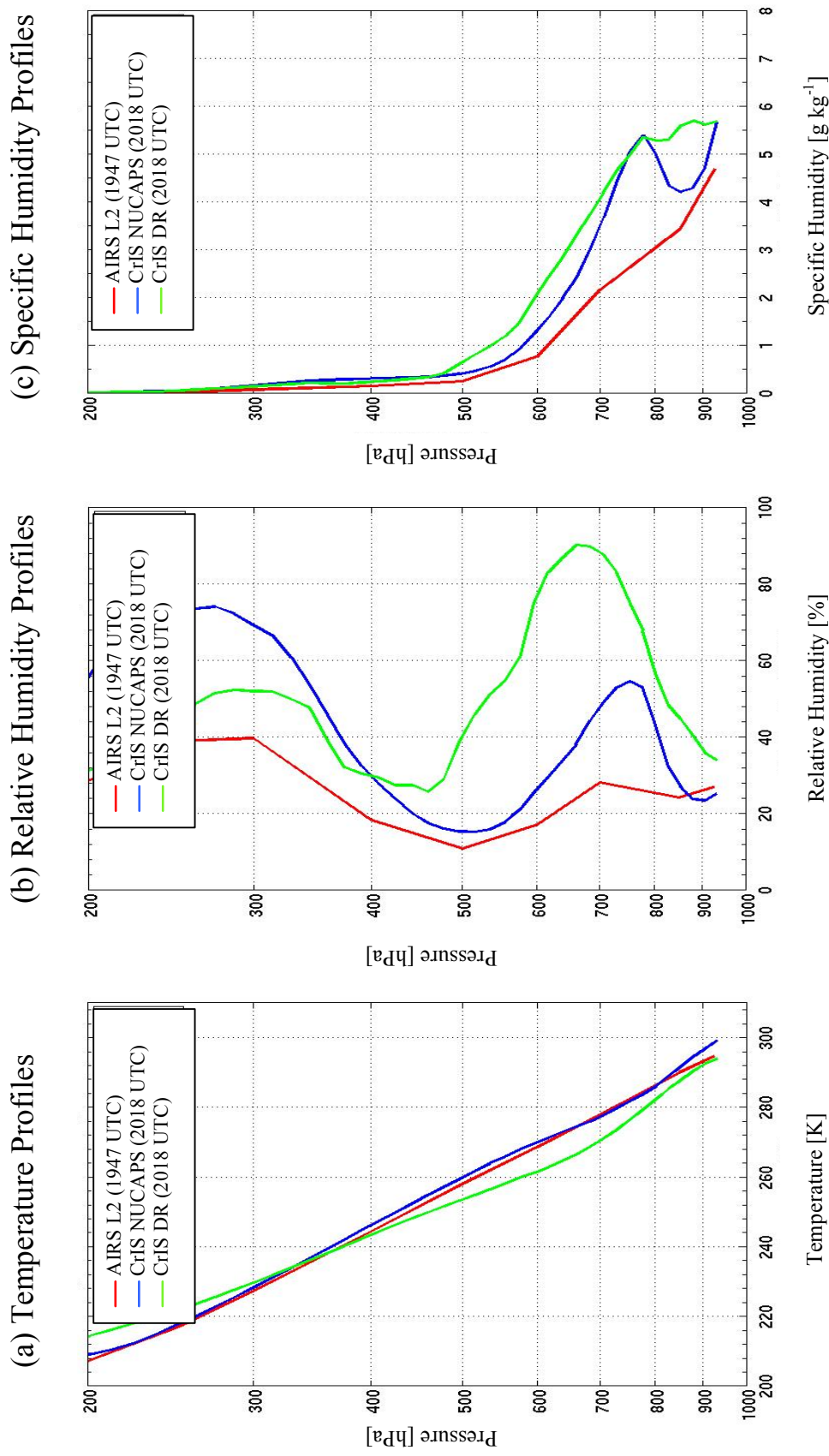


**Figure 20:** Retrieved profiles of (a) temperature, (b) relative humidity, and (c) specific humidity. Red profiles represent AIRS L2 retrieval at 1947 UTC, 03 May 2016. Blue profiles represent CrIS NUCAPS retrieval at 2018 UTC, 03 May 2016. Green profiles represent CrIS DR retrieval at 2018 UTC, 03 May 2016.

2018 UTC overpass of CrIS. The CrIS Dual Regression retrieved profiles are shown in green for the 2018 UTC overpass of CrIS. The Dual Regression algorithm was not applied to the AIRS overpass at 1947 UTC as it was deemed sufficient to have the AIRS L2 retrievals.

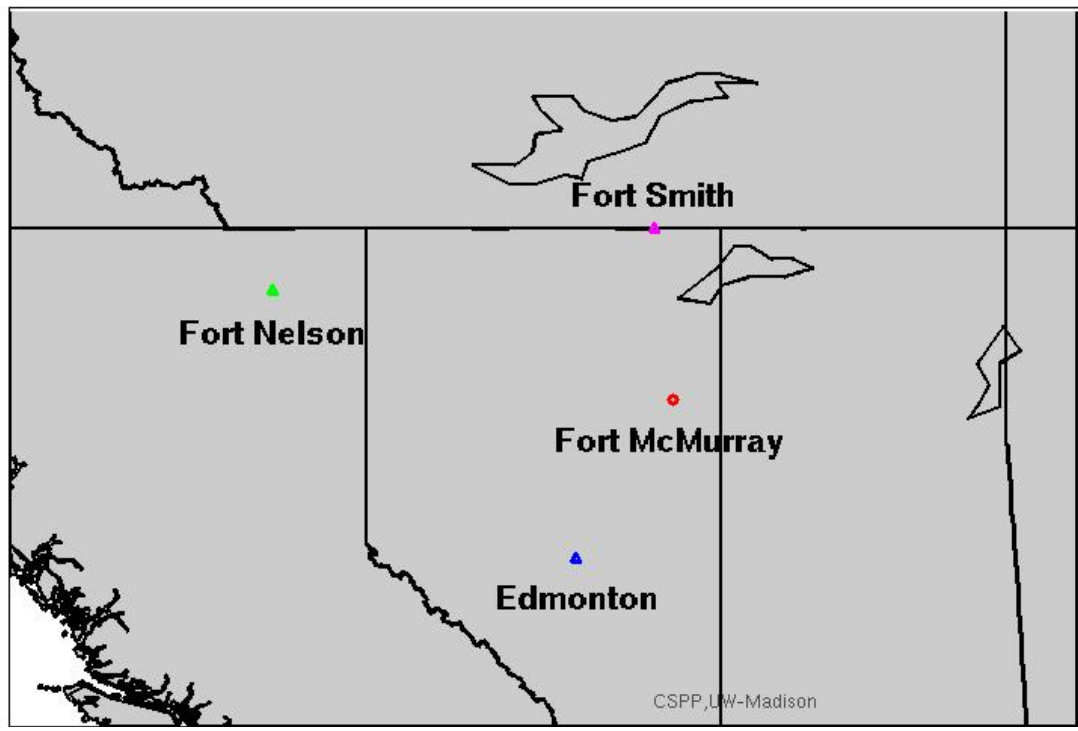
Recall that thirty minutes separate the AIRS overpass (red) from the CrIS overpass (blue and green). Surface temperatures between the two algorithms are relatively similar, with AIRS and NUCAPS with the highest precision nearing 296 K and the DR retrieval roughly 4 K warmer. This implies little change in surface temperatures between the two overpasses. Temperature structures throughout the vertical column are relatively consistent among the algorithms with the exception of Dual Regression showing cooler temperatures in the middle troposphere. Relative humidity profiles show an increase in mid-level humidity nearest 700-hPa between the AIRS and CrIS overpasses, implying a change within those thirty minutes. However, surface values of relative humidity between AIRS L2 and NUCAPS are very similar, both at approximately 28%, where DR surface values are just slightly higher, nearing 35%. The three algorithms feature comparable relative humidity structures throughout the atmospheric column, however, with AIRS L2 matching the aforementioned peaks in relative humidity near 700-hPa and minima near 500-hPa. Specific humidity profiles between the three algorithms vary immensely in the lower troposphere, with AIRS L2 featuring far less moisture at 700-hPa than both NUCAPS and DR. This implies an increase in mid-level moisture during the thirty minutes that separate the two overpasses, during which PyroCb development was evident. Additionally, the DR algorithm maintains a specific humidity value of roughly 5.5 g/kg throughout the boundary layer, where the NUCAPS retrieval dries out immediately above the surface before becoming more

moist around 700-hPa. Nevertheless, these profiles confirm the aforementioned warm surface temperatures and mid-level moisture signatures necessary for PyroCb enhancement.

Comparing retrieved profiles with radiosonde data, Fig. 21 shows the locations of the three nearest radiosonde launches to Fort McMurray. The average distance from each station to the wildfire is a staggering 484 kilometers. Thus, the radiosonde data for this particular case would in no way represent the conditions or the environment at Fort McMurray. Additionally, radiosonde launches are typically conducted at 0000 UTC and 1200 UTC each day, with an occasional special launch at 1800 UTC. For this case, the timing of the radiosondes would miss the PyroCb event entirely.

Nevertheless, comparisons of the AIRS overpass at 1947 UTC to each afternoon radiosonde are shown in Fig. 22 to demonstrate the benefit of hyperspectral retrievals in this case. In (a), the operational AIRS L2 retrieved temperature and dew-point temperature profiles are contrasted with an 1800 UTC radiosonde profile from Edmonton, located 235 miles to the southwest. The surface temperature at Edmonton is much warmer than at Fort McMurray, but the structures of the temperature profiles remain in close agreement to one another throughout much of the atmospheric column. Fluctuations between the two dew-point temperature profiles exist, however, throughout most of the troposphere. These differences are likely due to latitude, distance, and separation in time. In (b), the operational AIRS L2 retrieved temperature and dew-point temperature profiles, shown again in red, are contrasted with three 0000 UTC radiosonde profiles from Edmonton (blue), Fort Nelson (green), and Fort Smith (pink). Surface temperatures from all three 0000 UTC radiosondes are much warmer

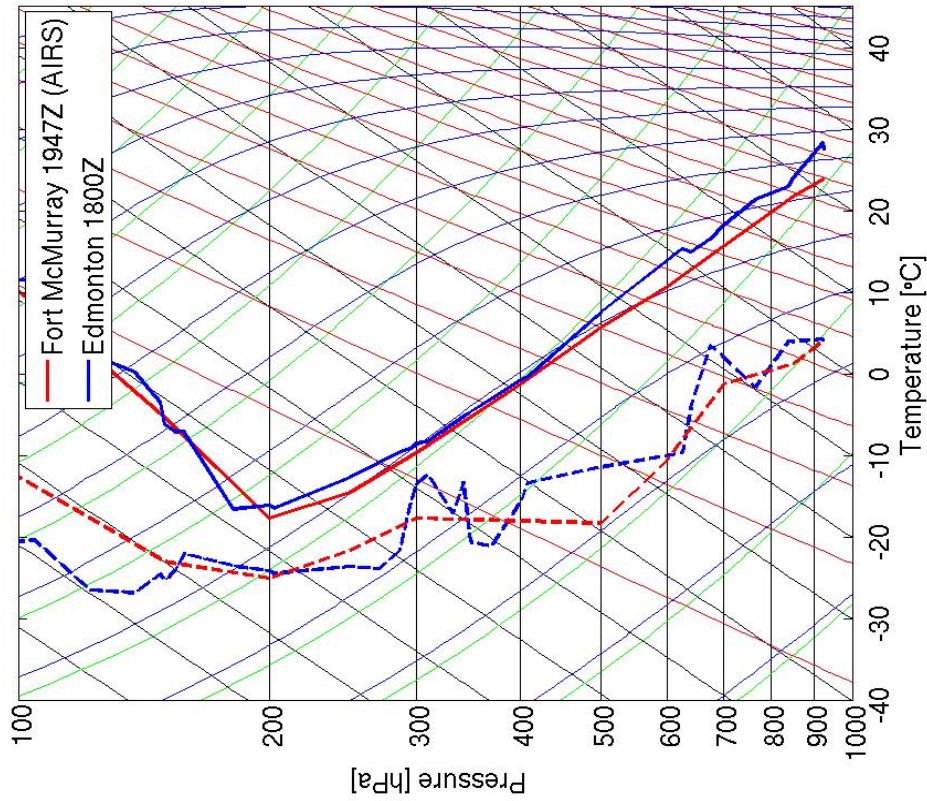
### Radiosonde Locations nearest Fort McMurray



<u>Distances from Fort McMurray to Radiosonde Locations</u>	
Fort McMurray (○) to Edmonton (▲)	= 378 km
Fort McMurray (○) to Fort Nelson (▲)	= 710 km
Fort McMurray (○) to Fort Smith (▲)	= 367 km
Average distance from Fort McMurray	= 484 km

**Figure 21:** Radiosonde locations nearest location of the Fort McMurray wildfire.

(a) AIRS Retrieval vs. 1800 UTC Edmonton Radiosonde



(b) AIRS Retrieval vs. 0000 UTC Radiosondes

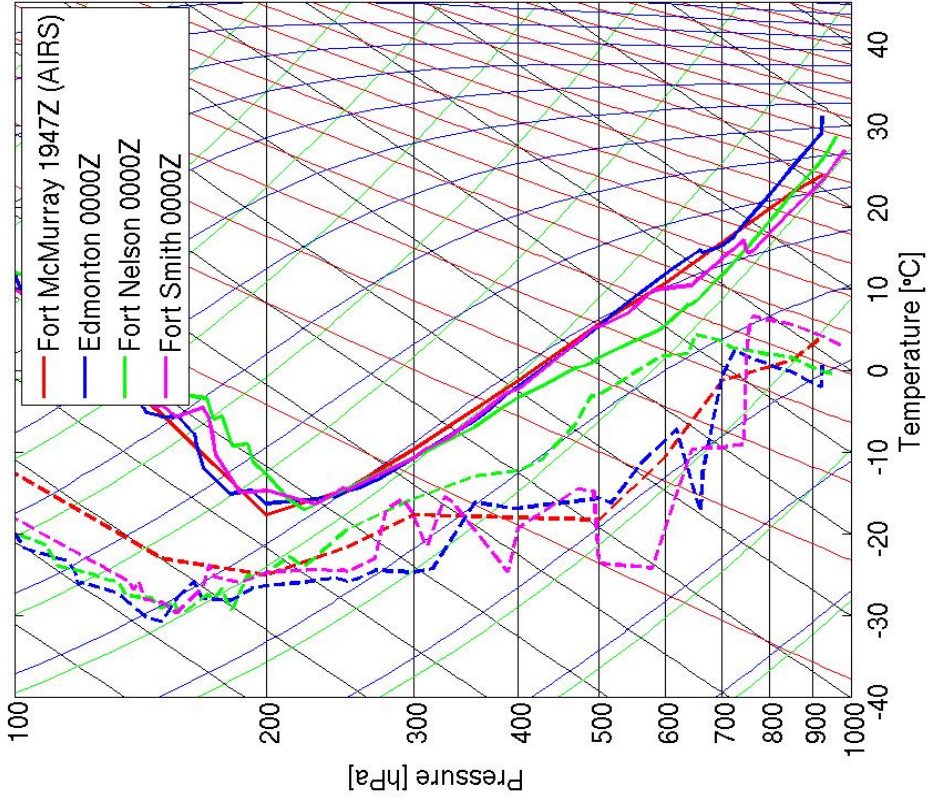


**Figure 22:** Skew-T diagram comparing the AIRS L2 retrieval of the AIRS 1947 UTC overpass to (a) an 1800 UTC radiosonde from Edmonton, and (b) 0000 UTC radiosondes from Edmonton, Fort Nelson, and Fort Smith. Solid profiles denote temperature. Dashed profiles denote dew-point temperature.

than the AIRS L2 retrieval, perhaps due to an increase in diurnal surface heating between 1947 UTC and 0000 UTC. With the exception of the AIRS retrieval, the lapse rates of the other three profiles are dry adiabatic in the lower-troposphere. Given the time of day, and one might anticipate that dry adiabatic layers would have formed. In general, retrieving accurate temperature and humidity profiles from infrared satellite measurements is most challenging near the surface, where the thermal contrasts between surface and atmospheric layers above is too small and knowledge of surface parameters like surface emissivity and surface skin temperature may be insufficient. Additionally, dew-point temperatures between the four profiles are seemingly divergent from one another throughout the atmospheric column, with the Fort Nelson profile featuring the moist moisture of the four, and the Fort Smith profile featuring the least moisture of the four.

The use of the WRF model to compare hyperspectral retrievals in closer temporal proximity to the PyroCb event is shown in Fig. 23, featuring 700-hPa mixing ratio at (a) 1800 UTC, (b) 1900 UTC, (c) 2000 UTC, and (d) 2100 UTC for 03 May 2016. It is important to note that the simulation provided by the WRF model does not incorporate the Fort McMurray wildfire, or the embedded PyroCb event. In Fig. 23, only values over  $2.4\text{-g kg}^{-1}$  are contoured. Across all four time periods, the WRF output shows that Fort McMurray lies in a region of relatively constant mixing ratio value of  $3.2\text{-g kg}^{-1}$ , with higher values above  $4\text{-g kg}^{-1}$  to the west and north. By 2100 UTC, this region of higher mixing ratios is advected upstream, closer to Fort McMurray, as a result of westerly flow. This suggests that the WRF simulation showed a similar synoptic setup favorable for moisture advection in the mid-troposphere.

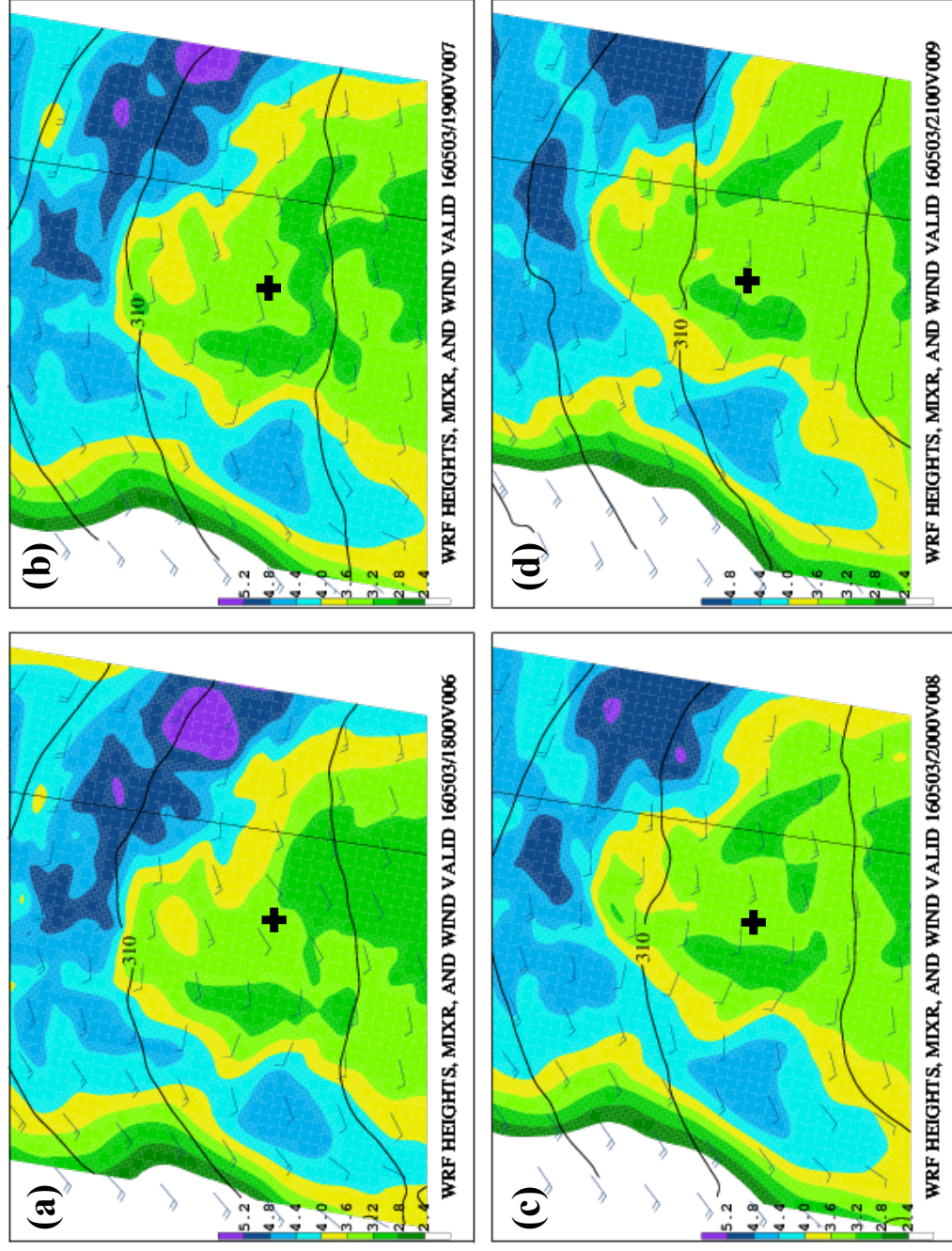


**Figure 23:** WRF model output, 03 May 2016, valid (a) 1800 UTC, (b) 1900 UTC, (c) 2000 UTC, and (d) 2100 UTC. Black contours denote 700-hPa geopotential height, contoured in 3-hPa intervals. Shading denotes mixing ratio, contoured in 0.4-g kg<sup>-1</sup> intervals from 2.4-g kg<sup>-1</sup> to 5.2-g kg<sup>-1</sup>. Wind barbs (blue) denote observed wind in kts. Black plus sign denotes location of Fort McMurray wildfire.

Figure 24 shows a skew-T diagram of a WRF sounding valid at 2000 UTC on 03 May, overlaid with the AIRS L2 retrieval valid at 1947 UTC. The WRF sounding shows surface temperatures near 24 °C, very similar to that of the AIRS L2 surface temperature of 23 °C just thirteen minutes earlier at 1947 UTC (seen on Fig. 22). The WRF sounding shows a slight near-surface temperature inversion that the AIRS L2 profile does not, but in all other regards, the profiles are strikingly similar. The profile of the WRF dew-point temperature also follows a similar structure to that of the AIRS L2 dew-point temperature, with a relative peak around 700-hPa and a relative pocket of drier air around 500-hPa. Thus, the WRF sounding compares favorably with the AIRS L2 retrieval, with a temporal difference of only thirteen minutes.

A time-height diagram is featured in Fig. 25, with a vertical profile of specific humidity in  $\text{g kg}^{-1}$  shown across seven hours, each hour from 1600 UTC to 2200 UTC on 3 May. There exists a nose of higher specific humidity of  $4.5 \text{ g kg}^{-1}$  near 750-hPa from 1600 UTC until approximately 2030 UTC, around the same time of the PyroCb event. Levels of surface moisture also increase dramatically following the event, rising nearly  $3 \text{ g/kg}$  from 2000 UTC to 2200 UTC. Analysis of this moisture evolution in the lower troposphere is insightful, as the WRF model does not simulate the Fort McMurray wildfire; in this simulation, the mid-tropospheric moisture exhaustion is still present without the wildfire or embedded PyroCb.

The hyperspectral sounder dataset proves useful in the case of the Fort McMurray wildfire as it provides an alternative method to analyze the atmospheric column when traditional radiosonde data does not collocate well in time or space. GEFS Reanalysis data

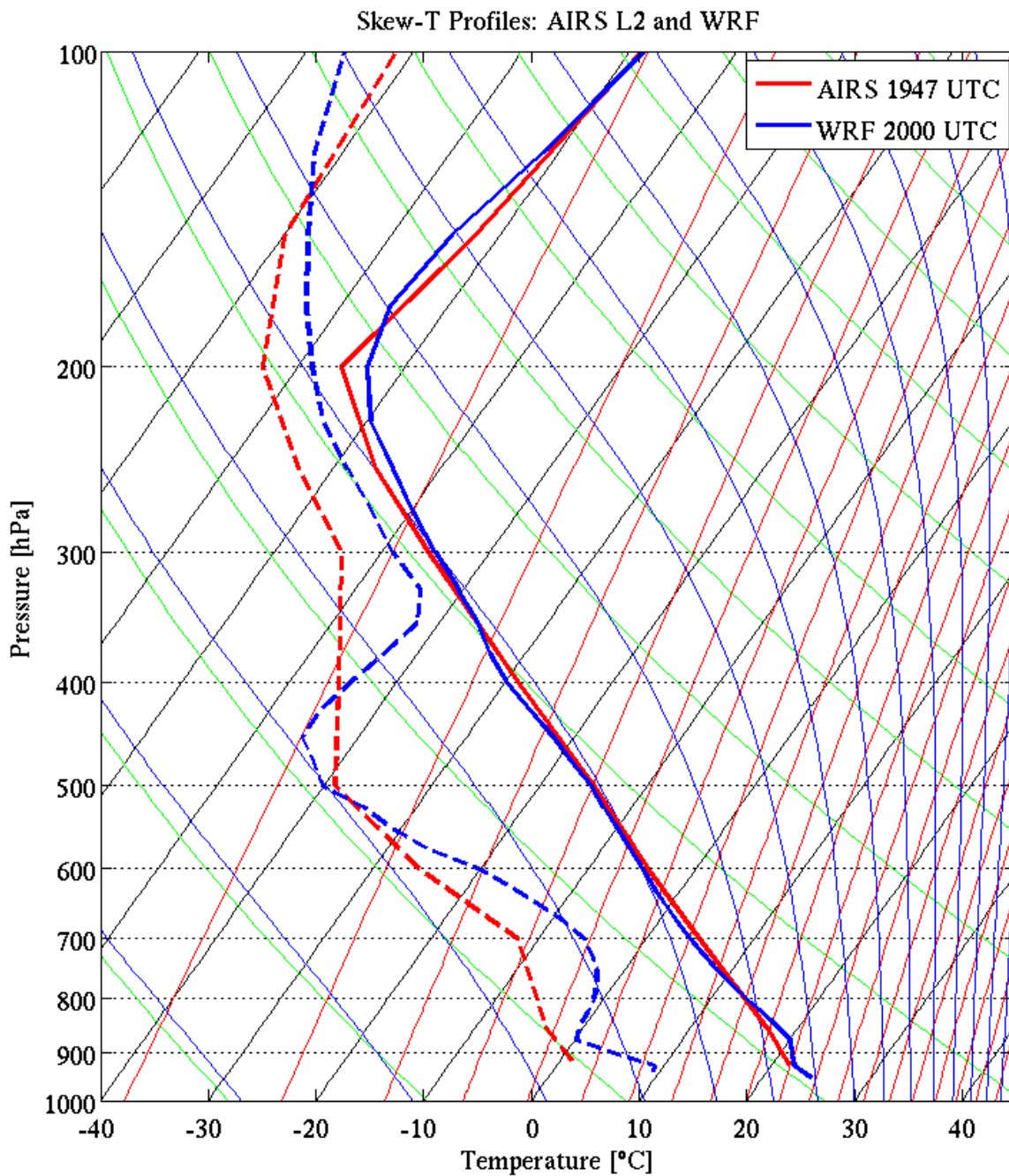


**Figure 24:** Skew-T diagram of AIRS L2 retrieval valid 1947 UTC (red) and WRF output valid 2000 UTC (blue) at location of Fort McMurray wildfire 03 May 2016. Solid lines indicate temperature in degrees Celsius. Dashed lines indicate dew-point temperature in degrees Celsius.

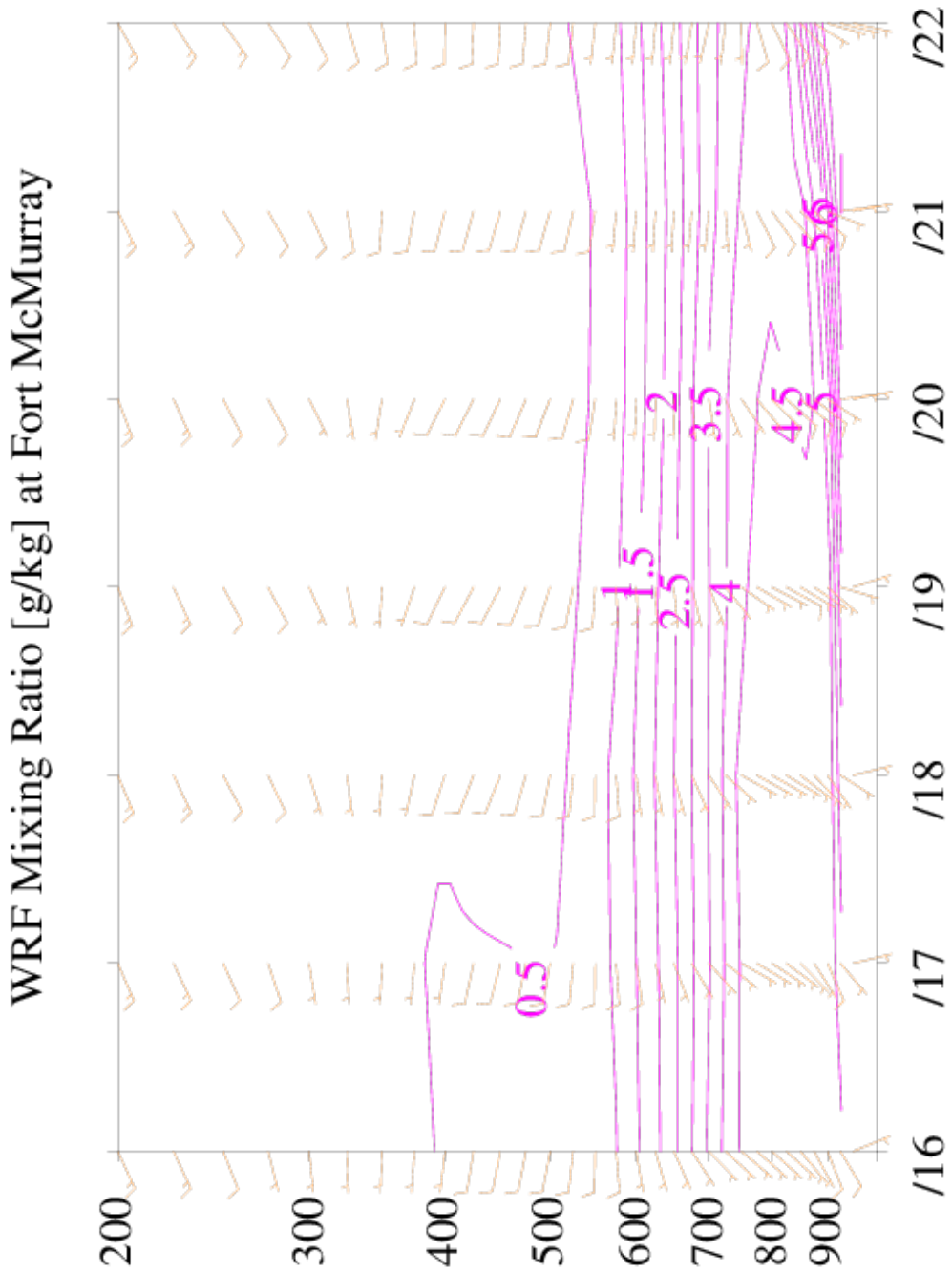


**Figure 25:** Time-height plot of hourly WRF output from 1600 UTC - 2200 UTC, 03 May 2016. Pink contours denote mixing ratio, in  $\text{g kg}^{-1}$ , contoured in  $0.5\text{-g kg}^{-1}$  intervals. Orange wind barbs denote observed winds in kts.

showed the synoptic environment characterized by a strong 500-hPa geopotential height ridge, not entirely consistent with Dr. Peterson's "Canadian Ridge Breakdown" classification scheme as the ridge had not broken down by the time of the PyroCb. Hyperspectral brightness temperatures showed the Fort McMurray PyroCb developed in a region of high, cool clouds, with window region temperatures below 250 K and a signature consistent spatially with the PyroCb detected on visible imagery. Differences in the three retrieval algorithms were presented, but similar structures in vertical profiles between the three showed strong agreement of warm surface temperatures, relative peaks in relative humidity near 700-hPa, and similar specific humidity values throughout much of the troposphere. The WRF model provided spatially and temporally proximate simulations of the PyroCb event environment, suggesting a similar presence of mid-level moisture to that shown by hyperspectral retrievals. Additionally, a WRF sounding valid only thirteen minutes apart from the AIRS overpass showed strong collocation to the AIRS L2 retrieved profile, suggesting that the model handled the development of the PyroCb environment very well.

## 5 Summary and Conclusions

Hyperspectral sounders provide a valuable dataset from which profiles of temperature and moisture at high vertical resolution may be retrieved. With four hyperspectral sounders currently aboard separate polar-orbiting satellites, the time evolution of atmospheric phenomena and associated processes can be readily analyzed. Hyperspectral sounder data is most useful in its twice per day availability over every location on the planet, proving most useful in remote regions where components of traditional in-situ observation networks are sparse or nonexistent. Most specifically, hyperspectral sounder data is greatly beneficial in the study of PyroCb events, where short lifetimes and remote locations typically make them difficult to analyze. In this study, hyperspectral sounder applications were used to investigate two PyroCb events, the Yarnell Hill wildfire in Arizona and the Fort McMurray wildfire in Alberta, Canada.

Prior to using the data, a solid foundational understanding of remote sensing and atmospheric radiation is crucial. Chapter 2 of this study presented the necessary equations of Planck function, Wien displacement, upwelling radiation, weighting function, and brightness temperature to better understand how an instrument measures radiation. Also presented in this section were in-depth descriptions of the three hyperspectral sounders in orbit: AIRS, IASI, and CrIS. Additionally, Chapter 2 provided an introduction to PyroCb activity and presented the three synoptic classification schemes (Peterson, 2017b).

Chapter 3 of this study provided an introduction to linear regression and physical optimal estimation as methods for retrieval of atmospheric profiles and parameters from hyperspectral radiances, presenting equations for the linear regression model and regression

coefficients, as well as for the physical optimal estimation solution and error covariance. These techniques were applied in explanation of the three retrieval algorithms used in this study: Dual Regression, NUCAPS, and AIRS L2 Standard Physical Retrieval. Also presented in Chapter 3 was a background of the WRF model for additional simulation of the Fort McMurray case study, as well as other data sources used in the two case studies.

Hyperspectral sounder data associated to the Yarnell Hill wildfire of June 2013 was investigated in attempt to characterize the environment prior to a PyroCb event, specifically one detected via visible imagery at 2345 UTC on 30 June. Hyperspectral brightness temperatures confirmed an incoming convective system from the northeast, and showed cooler temperatures in the window region over Yarnell, suggesting cloudy-sky conditions. Profiles of temperature and moisture retrieved using the Dual Regression algorithm confirmed very warm surface temperatures over 300 K, with dry conditions at the surface but an increase in both relative and specific humidity values near 700-hPa. Comparison with radiosonde data from Flagstaff, Arizona at 0000 UTC on 1 July to the last satellite overpass of the afternoon was made, but strong disparity in time and space made such a comparison difficult. Situated at a low latitude, the location of the Yarnell wildfire was not favorable with the given satellite overpasses of 30 June, making the use of hyperspectral sounder data slightly more difficult in this case. Nevertheless, the hyperspectral sounder dataset provided information regarding the environment antecedent to the PyroCb that would otherwise not have been provided from radiosonde data.

Hyperspectral sounder data was also investigated for the Fort McMurray wildfire in far northern Alberta, Canada in May 2016 to characterize the environment leading up to a PyroCb event detected on visible imagery around 1945 UTC on 03 May. Brightness

temperature spectra showed cool temperatures in the window region, confirming the location of the PyroCb among high, cool clouds in the region, and the overshooting top signature of the PyroCb was confirmed upon analysis of spatial brightness temperatures. Retrieved profiles of temperature and moisture were presented using three different retrieval algorithms, and while each had its own distinct differences, the relative structures were similar in showing very warm surface temperatures and a surge of moisture near 700-hPa. Comparison with radiosonde data in this case was again difficult, as the average distance of the three nearest radiosonde locations to the location of the Fort McMurray wildfire was almost five hundred kilometers. This proves the value of the hyperspectral sounder dataset as it provides observations in a region where radiosonde data would miss the PyroCb event entirely. The use of the WRF model provided high resolution in space and time simulation data for this case, with model output of mixing ratio two hours prior and after the PyroCb event showing the setup for moisture advection by a westerly wind. There can be no conclusions drawn about the effect of the moisture content on the PyroCb in this case, however, as the model does not simulate the wildfire or the associated PyroCb. Additionally, a 2000 UTC sounding from the WRF model shows that the model was in close agreement with the AIRS retrieval algorithm, featuring a slightly moist adiabatic lapse rate through the lower troposphere. Lastly, a time-height diagram of mixing ratio showed an exhaustion of moisture near 750-hPa in close timing to the PyroCb event that was not simulated by the model.

It is important to note that while hyperspectral sounder data is never meant to replace any existing source of in-situ observations, it can greatly enhance and complement other sources when analyzing the environments of various atmospheric phenomena. The high

spectral resolution of the instruments translates to high vertical resolution of temperature and moisture profiles, which are used as valuable tools in nowcasting, weather forecasting and numerical weather prediction. The conjunction of hyperspectral sounder data with a widely understudied phenomenon like a PyroCb event proves incredibly valuable, expanding both the use of hyperspectral sounder data and the understanding of PyroCb activity, both ultimate goals with sizeable implications within the atmospheric science community.

## References

- Bachmeier, S., 2013: Yarnell Hill fire in Arizona. *CIMSS PyroCb Blog*.
- , 2016: Fort McMurray, Alberta Wildfire. *CIMSS PyroCb Blog*.
- Fromm, M. D., D. Lindsey, R. Servranckx, G. Yue, T. Trickl, R. Sica, P. Doucet, and S. Godin-Beekmann, 2010: The untold story of pyrocumulonimbus. *Bull. Amer. Meteor. Soc.*, **91**, 1193-1209.
- , R. H. D. McRae, J. J. Sharples, and G.P. Kablick III, 2012: Pyrocumulonimbus pair in Wollemi and Blue Mountains National Parks, 22 November 2016. *Aust. Meteor. Oceanogr. J.*, **62**, 117-126.
- Gelb, A., editor, 1974: Applied optimal estimation. Massachusetts Institute of Technology Press, Cambridge, Massachusetts, pp. 2-3.
- Gambacorta, A., C. Barnet, W. Wolf, M. Goldberg, T. King, X. Ziong, N. Nalli, E. Maddy, and M. Divakarla, 2012: The NOAA unique CrIS/ATMS processing system (NUCAPS): First light retrieval results. Proceedings of the ITWG Meeting, ITWG, Toulouse, France.
- Goldberg, M. D., Y. Qu, L. M. McMillin, W. Wolf, Lihang Zhou, and M. Divakarla, 2003: AIRS near-real-time products and algorithms in support of operational numerical weather prediction. *IEEE Transactions on Geoscience and Remote Sensing*, **41**, pp. 379-389.
- Hardy, K., and L. K. Comfort, 2014: Dynamic decision processes in complex, high-risk operations: The Yarnell Hill Fire, Jun 30, 2013. *Safety Science*, **71**, 39-47.

- Huang, H.-L., and P. Antonelli, 2001: Application of principal component analysis to high-resolution infrared measurement compression and retrieval. *J. Appl. Meteor.*, **40**, 365-388.
- Kalman, R. E., 1960: A new approach to linear filtering and prediction problems. *Trans. AMSE, Ser. D, J. Basic Eng.*, **49**, 1004.
- Kaplan, L. D., 1959: Inference of atmospheric structure from remote radiation measurements. *J. Opt. Soc. Am.*, **49**, 1004-1014.
- King, J. I. F., 1956: The radiative heat transfer of planet earth. *Scientific Use of Earth Satellites*, University of Michigan Press, Ann Arbor, Michigan, pp. 133-136.
- Menzel, W. P., 2006: Remote sensing applications with meteorological satellites. University of Wisconsin-Madison, Madison, WI.
- Nau, R., 2014: Notes on linear regression analysis. Fuqua School of Business, Duke University, Durham, North Carolina, pp. 1-18.
- Peterson, D., E. J. Hyer, J. R. Campbell, M. D. Fromm, J. W. Hair, C. F. Butler, and M. A. Fenn, 2015: The 2013 Rim Fire: Implications for predicting extreme fire spread, pyroconvection, and smoke emissions. *Bull. Amer. Meteor. Soc.*, **96**, 229-247.
- , M. D. Fromm, J. Solbrig, E. J. Hyer, M. Surratt, and J. R. Campbell, 2017a: Detection and Inventory of Intense Pyroconvection in Western North America using GOES-15 Daytime Infrared Data. *J. Appl. Meteor.*, **56**, 471-493.
- , E. J. Hyer, J. R. Campbell, J. E. Solbrig, and M. D. Fromm, 2017b: A Conceptual Model for Development of Intense Pyrocumulonimbus in Western North America. *Mon. Wea. Rev.*, **145**, 2235-2255.
- Petty, G. W., 2006: A first course in atmospheric radiation. Sundog Pub., Madison, WI.

- Rodgers, C., 2000: Inverse methods for atmospheric sounding: Theory and practice. World Scientific Publishing Co., 240 pp.
- Skamarock, W. C., Klemp, J. B., J. Dudhia, D. O. Gill, D. M. Barker, W. Wang, and J. G. Powers, 2005: A description of the advanced research WRF version 2. *NCAR Technical Note*, pp. 1-101.
- Smith, W. L., H. M. Woolf, and W. J. Jacob, 1970: A regression method for obtaining real time temperature and geopotential height profiles from satellite spectrometer measurements and its application to Nimbus-III "SIRS" observations. *Mon. Wea. Rev.*, 98, 582-603.
- , E. Weisz, S. Kirev, D. K. Zhou, Z. Li, and E. E. Borbas, 2012: Dual-regression retrieval algorithm for real-time processing of satellite ultraspectral radiances. *J. Appl. Meteor. Climatol.*, 51, 1455-1476.
- Weisz, E., H.-L. Huang, J. Li, E. Borbas, K. Baggett, P. Thapliyal, L. Guan, 2007: International MODIS and AIRS processing package: AIRS products and applications. *Journal of Applied Remote Sensing*, 1, 013519.
- , W. L. Smith, J. Li, W. P. Menzel, and N. Smith, 2011: Improved profile and cloud top height retrieval by using dual-regression on high-spectral resolution measurements, paper (HWA4) presented at the OSA topical meeting: Hyperspectral Imaging and Sounding of the Environment (HISE), Toronto, Canada.
- , W. L. Smith, and N. Smith, 2013: Advances in simultaneous atmospheric profile and cloud parameter regression based retrieval from high-spectral resolution measurements. *J. Geophys. Res. Atmos.*, 118, 6433-6443.

- , N. Smith, and W. L. Smith, 2015a: The use of hyperspectral sounding information to monitor atmospheric tendencies leading to severe local storms. *Earth and Space Sci.*, **2**, 1-9.
- , N. Smith, W. L. Smith, K. Strabala, and A. Huang, 2015b: Assessing hyperspectral retrieval algorithms and their products for use in direct broadcast applications. 20<sup>th</sup> International TOVS Study Conference (ITSC-20), 28 October – 3 November 2015, Lake Geneva, Wisconsin, USA; proceedings paper 3.03. Available at [http://cimss.ssec.wisc.edu/hiresdb/resources/pub/files/papers/AssessingHSRetr\\_Weisz\\_ITSC20\\_2015.pdf](http://cimss.ssec.wisc.edu/hiresdb/resources/pub/files/papers/AssessingHSRetr_Weisz_ITSC20_2015.pdf).
- Zhou, D. K., W. L. Smith Sr., X. Liu, A. M. Larar, S. A. Mango, and H.-L. Huang, 2007: Physically retrieving cloud and thermodynamic parameters from ultraspectral IR measurements. *J. Atmos. Sci.*, **64**, 969-982.